Università degli Studi di Padova

Dipartimento di Ingegneria Industriale
Corso di Laurea in Ingegneria Meccanica

Tesi di Laurea Magistrale

Development of an Unsteady BEM Code for Wind Turbine Applications

Relatore:
Prof. Ernesto Benini

Laureando:
Raffaele Peraro

Correlatori:
Ing. Andrea Dal Monte
Ing. Luca Menegozzo

Anno accademico 2018/2019

Ringrazio di cuore la mia famiglia per avermi supportato ed incoraggiato in ogni momento del mio non sempre facile percorso di studi. Un pensiero va ai miei cari nonni nonché agli amici di una vita per le tante serate passate assieme ed, immancabilmente, al gruppo parole. Desidero ringraziare profondamente il prof. Benini per tutto ciò che mi ha insegnato, per avermi trasmesso durante i suoi corsi la passione per le macchine, per l'opportunità e per i consigli che mi ha dato nel percorso di tesi; la sua professionalità ed umanità costituiranno per me un esempio costante a cui ispirarmi per il futuro. Ringrazio fortemente Andrea e Luca per la loro massima competenza, per avermi trasmesso un metodo di lavoro efficace ed utile per il domani, per i mille suggerimenti che mi hanno dato e per aver sempre creduto nelle mie capacità.

A Ginevra.

Nomenclature

a $[-]$	Axial induction factor	Re $[-]$	Reynolds number
a' $[-]$	Tangential induction factor	R_{hub} $[m]$	Rotor hub radius
a_{yaw} $[-]$	Yawed axial induction factor	R_{tip} $[m]$	Rotor tip radius
A $[m^2]$	Section area	T $[N]$	Thrust
B $[-]$	Number of blades	u $[m/s]$	Wind speed at rotor plane
c $[m]$	Chord length	u_1 $[m/s]$	Wind speed in the wake
C_l, C_l^{st} $[-]$	Static lift coefficient	V_{blade} $[m/s]$	Blade section velocity
C_l^{dyn} $[-]$	Dynamic lift coefficient	V_{rel} $[m/s]$	Relative velocity
C_l^{fs} $[-]$	Fully separated lift coefficient	V_{rot} $[m/s]$	Rotational velocity
$C_{l,\alpha}$ $[-]$	Slope of lift curve	V_{tang} $[m/s]$	Tangential velocity
C_d $[-]$	Drag coefficient	V_0 $[m/s]$	Wind speed
C_m $[-]$	Moment coefficient	W $[m/s]$	Induced velocity
C_n $[-]$	Normalized normal force	α $[rad]$	Angle of attack
C_P $[-]$	Power coefficient	$\bar{\alpha}$ $[rad]$	Starting extrapolation angle
C_t $[-]$	Normalized tangential force	α_0 $[rad]$	Angle of attack at zero lift
C_T $[-]$	Thrust coefficient	β $[rad]$	Blade twist
C_θ $[m/s]$	Rotational velocity in the wake	Γ $[m^2/s]$	Strength of vortex filament
dsq $[kW]$	Distance function	Δt $[s]$	Time step
D $[N/m]$	Drag per unit lenght	ϵ $[-]$	Convergence tolerance
f_s $[-]$	Dynamic separation function	θ $[rad]$	Blade local pitch
f_s^{st} $[-]$	Static separation function	θ_{az} $[rad]$	Azimuth angle
F_N $[N/m^2]$	Normal force per unit area	θ_{cone} $[rad]$	Cone angle
L $[N/m]$	Lift per unit lenght	θ_p $[rad]$	Blade global pitch angle
$\dot{m}$ $[kg/s]$	Mass flow rate	θ_{yaw} $[rad]$	Yaw angle
M $[Nm/m]$	Moment per unit lenght	λ $[-]$	Relaxation parameter
p_N $[N/m]$	Normal force per unit lenght	μ $[Pa\ s]$	Kinematic viscosity
p_T $[N/m]$	Tangential force per unit lenght	ρ $[kg/m^3]$	Air density
P $[W]$	Power	σ $[-]$	Solidity
P_{BEM} $[W]$	BEM interpolated power	τ $[s]$	Time constant
P_{exper} $[W]$	Experimental power	ϕ $[rad]$	Flow angle
P_{max} $[W]$	Maximum available power	χ $[rad]$	Skew angle
r $[m]$	Radial position	ω $[rad/s]$	Rotor angular velocity
R $[m]$	Rotor radius	ω_{red} $[-]$	Reduced frequency

Contents

Summary

Wind turbines are a clean alternative to conventional fossil fuel-based power production plants. Despite technological advancements in the last decades, the unsteady aerodynamics of the machine is still poorly understood and developed: therefore it is still a challenging step to improve design codes in order to predict the unsteady interaction between machine and airflow.

The present work aims to improve and validate an existing code [1] for wind turbine applications, based on the unsteady Blade Element Momentum theory (BEM), in order to study the aerodynamic behaviour of the machine under unsteady flow conditions. In particular the objectives of this thesis are:

- creation of wide dataset of polar diagrams;
- implementation of a yaw model routine;
- implementation of a dynamic stall routine.

The commercial software MATLAB has been chosen as a development environment for the unsteady BEM code. Although high-fidelity techniques, as the Computational Fluid Dynamics (CFD), are more realible for strongly 3D and separated flow, a greater effort on meshing, boundary conditions setting and computational cost are required. For these reasons, low-fidelity models, such as the BEM approach, still represent a widely employed calculation strategy, since they join an accurate performance prediction and a low computational cost.

A necessary overwiev about BEM algorithm is reported in Chapter 1. An improvement in polar diagrams calculation is presented in Chapter 2 and included in the BEM code, after a validation using the experimental power curves of AOC 15/50 and NREL Phase VI horizontal-axis wind turbines (HAWTs). The general structure of the unsteady BEM code (UBEM) is illustrated in Chapter 3, where the sources of unsteady phoenomena are investigated and the routines which compose the algorithm are summarized. The results of the simulations for yawed flow are discussed in Chapter 4, referring to the low speed shaft torque and to the normal force spanwise measurements. Finally, the implementation of a dynamic stall model is presented in Chapter 5, in which a validation using various experimental results on pitching oscillating airfoils by NREL is proposed.

Riassunto esteso

Tra le macchine per la produzione di energia rinnovabile, le turbine eoliche rappresentano la principale alternativa ai tradizionali impianti basati sull'utilizzo di combustibili fossili. Sebbene i recenti sviluppi nello studio di modelli di calcolo in ambito eolico, l'aerodinamica non stazionaria della macchina risulta tuttora poco approfondita: è pertanto motivo di sfida il miglioramento e lo sviluppo di nuovi codici computazionali a carattere tempo-variante, al fine di comprendere la complessa interazione tra macchina ed flusso d'aria.

Il presente lavoro si pone come obiettivo il miglioramento e la validazione di un codice di calcolo esistente [1] per turbine eoliche, basato su un approccio BEM (Blade Element Momentum) non stazionario, con lo scopo di studiare l'aerodinamica della macchina in condizioni di corrente non stazionaria. In particolare gli obiettivi di tale tesi sono:

- creazione di un ampio database di polari;
- implementazione di un modello di yaw;
- implementazione di un modello di stallo dinamico.

Come ambiente di sviluppo per il codice BEM non stazionario è stato scelto il software commerciale MATLAB. Nonostante le moderne tecniche di calcolo high-fidelity, quali la fluidodinamica computazionale (CFD), sembrino rivelarsi più appropriate per l'indagine di flussi fortemente tridimensionali ed in condizioni di separazione, tali metodologie richiedono particolare attenzione sia in fase di creazione della griglia di calcolo (meshing), che di impostazione delle condizioni al contorno (boundary conditions setting), nonché necessitano di un maggior sforzo computazionale. Per tali ragioni, i modelli aerodinamici low-fidelity con approccio BEM rappresentano tuttora uno strumento di calcolo largamente impiegato, poiché garantiscono un'accurata stima delle prestazioni e nel contempo un modesto sforzo computazionale.

Una necessaria panoramica sull'algoritmo BEM è riportata nel Capitolo 1. Un miglioramento nel calcolo delle polari dei profili aerodinamici è presentato nel Capitolo 2 ed incluso nel codice BEM, in seguito ad un'accurata validazione sulle curve sperimentali di potenza per le turbine ad asse orizzontale AOC 15/50 e NREL Phase VI. La struttura generale del codice BEM unsteady (UBEM) è illustrata nel Capitolo 3, nel quale sono approfondite le cause dei fenomeni non stazionari coinvolti e sono riassunte le routines di calcolo che compongono l'algoritmo. I risultati delle simulazioni per flusso non ortogonale al rotore (yawed flow) sono discussi nel Capitolo 4, con riferimento a misurazioni di coppia all'albero di bassa velocità e di misure radiali di forza normale. Infine, l'implementazione di un modello di stallo dinamico per applicazioni eoliche è presentato nel Capitolo 5, in cui il processo di validazione è portato a termine grazie all'utilizzo di risultati sperimentali condotti da NREL su profili aerodinamici oscillanti.

- I -

Introduction

The purposes of the following chapter are to give a brief review of wind power technology, a summary of operating principles of wind turbines and a detailed explanation of Blade Element Momentum method.

1.1 Wind power

Increasing the power production coming from alternative energy sources is one of the most important challenges of 21^{th} century, to reduce the impact of human activities and economy on the enviroment. Fossil fuel consumption significantly contributes to many issues, such as air pollution, exploitation of land sources, greenhouse effects and global warming. Therefore, both for environmental reasons and the need of each country for an increased self-sufficiency in energy production, electricity from wind is a green, reliable and efficient alternative source of power.

1.1.1 Historical review

In the following subsection, some of the major milestones in wind power development are mentioned. Historically, the most important usage of wind was the propulsion of ships with sails before the Industrial Revolution. Wind had also been used in windmills to grind grain or to pump water for irrigation or, as in the Netherlands, to prevent the ocean from flooding low lying land.

At the beginning of the 20^{th} century electricity gradually spread both in industries and houses; the first electrical grids consisted of low voltage DC cables with high losses, therefore electricity had to be generated close to the site of use. On farms, small wind turbines were ideal for this purpose and the danish Poul la Cour, who was among the first to connect a windmill to a generator, gave a so called course for agricultural electricians. An example of La Cour's great foresight was the installation in his school of the first wind tunnels in the world, in order to investigate rotor aerodynamics. However, fossil fuel sources took over in the production of electricity, thanks to Diesel engines and steam turbines; only during Second War World the wind power usage flourished again due to scarse fuel supply. Afterwards, the development of more efficient wind turbines was still carried on in several countries, especially in Northern and Western Europe, such as France, UK and Denmark, and in the USA. A great contribution in the earliest development of

wind power was given by Johannes Juul and by a former student of la Cour. In the mid $1950s$, Juul introduced the so called Danish concept, by constructing the Gedser turbine, shown in Figure 1.1. It was characterized by a three-bladed rotor connected to an AC asynchronous generator, running at almost constant speed, upwind configuration and stall regulated.

During the oil crisis in 1973, many countries wanted to be less dependent on oil imports, so more attention on new sources of energy, such as wind power, became interesting again. Many national research programs were initiated in order to investigate the possibilities of wind energy availment; large prototypes were built as test cases to evaluate the economics of electricity from wind and to measure loads on big wind turbines. Commercial wind turbines have gradually become an important industry with an annual turnover in the $1990s$ of more than a billion US dollars per year.

Figure 1.1: *Gedser wind turbine - Energy Museum Bjerringbro.*

1.1.2 Wind energy in Europe 2018

A quantitative and detailed description about spread, development and economics of wind turbines in Europe in 2018 is given in [2]: this report summarises the new plant installations and financing activity in Europe's wind farms from 1 January to 31 December 2018. Europe installed 11.7 GW (10.1 GW in EU-28) of new wind power in 2018, this is a decrease of 32% compared to 2017. Europe decommissioned 0.4 GW of wind turbines, so the net increase in Europe's wind energy capacity in 2018 was 11.3 GW. Wind energy remains the second largest form of power generation capacity in the EU-28 and is likely to overtake natural gas installations in 2019, as shown in Figure 1.2. It is important to remark that nowadays in Europe:

- the wind power capacity installed is 170 GW onshore and 19 GW offshore, more details are given by Figure 1.3;
- wind energy accounts for 18.8% of total installed power generation capacity;
- conventional power sources such as fuel, oil and coal continue to decrease their capacity, new natural gas and coal installations have reached a low record of 0.9

GW additions.

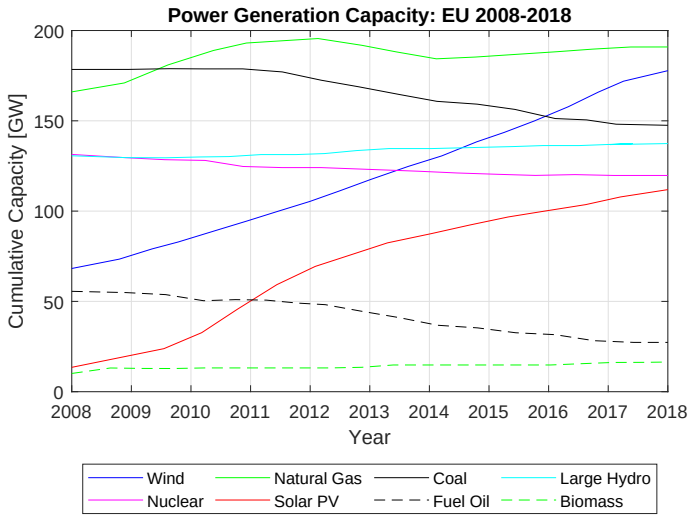

Figure 1.2: *Total power generation capacity in EU [2].*

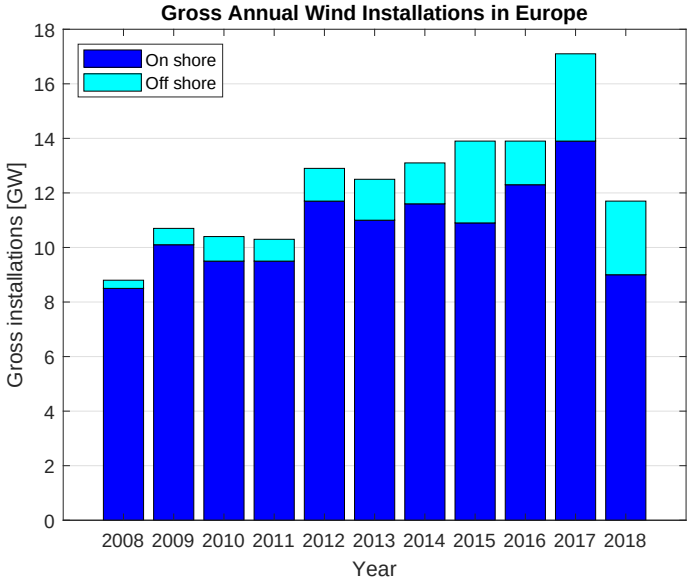

Figure 1.3: *Site of gross wind energy production [2].*

From a geographical point of view, Germany has the largest installed wind power capacity in 2018, with 29% of Europe's gross installations, but its new installations were down of 49% in 2017. Spain, UK and France has followed Germany in terms of largest installed wind power capacity; Italy, Sweden, Turkey, Poland, Denmark and Portugal have more than 5 *GW* of wind installations. Denmark is the country with the highest share of wind energy in its electricity demand, 41%. UK has registered the largest annual increase of wind energy in its electricity demand, from 13.5% to 18%. Ireland (28%), Portugal (24%), Germany (21%) and Spain (19%) are the other countries with the highest share of wind in their electricity mix. Finally, a pie chart of billion euros, *€bn*, invested in renewable energy in 2018 is represented in Figure 1.4: 26.7*€bn* have been invested in wind energy, 16.3*€bn* onshore and 10.3*€bn* offshore.

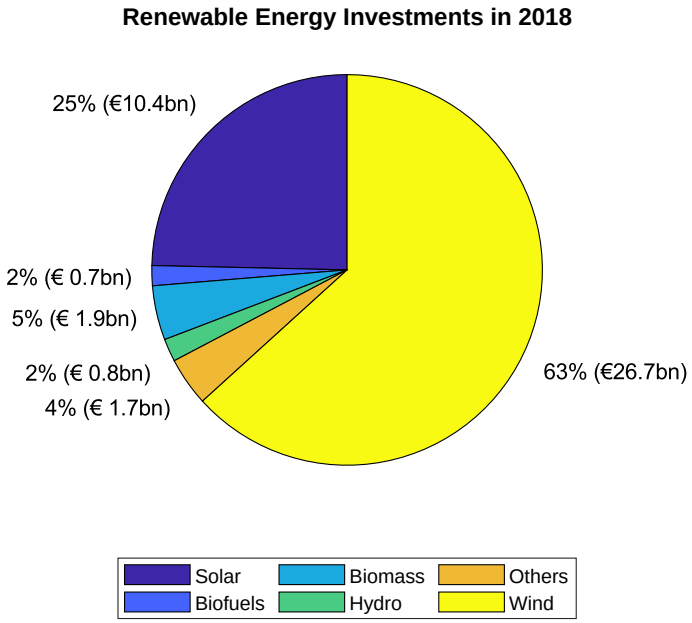

Figure 1.4: *Amount of €bn invested in renewable energy in 2018 [2].*

1.2 Main features of wind turbines

Wind turbines transform the kinetic energy of the wind into mechanical energy available to a shaft and finally into electrical energy thanks to a generator. Theoretically, the maximum available power is obtained from energy conservation if the wind speed could be reduced to zero:

$$P_{max} = \frac{1}{2}\dot{m}V_0^2 = \frac{1}{2}\rho A V_0^3 \tag{1.1}$$

Equation 1.1 for the maximum available power shows that power increases with the cube of the wind speed, as affirmed by the Mechanical Similitude Theory, and only linearly with density and area. For wind turbine applications density is considered constant, due to the absence of appreciable compressibility effects, as Mach number is lower than 0.3. In practice, wind velocity cannot be reduced to zero, so a power coefficient is defined as:

$$C_P = \frac{P}{P_{max}} \tag{1.2}$$

As explained in [3], a theoretical maximum for power coefficient does exist and it is denoted as the Betz limit, whose value is $C_{Pmax} = 16/27 = 0.593$. Modern wind turbines are designed by optimizing criteria to operate as close as possible to the Betz limit, and nowadays a value for power coefficient close to the limit is reached. The power production deeply depends on the installation site, therefore wind speed is first measured over a period of time to obtain accurate values. Many statistics have been given on different wind turbines sited in Denmark: as a rule of thumb they produce approximately $1000kWh/(m^2year)$.

Modern wind turbines consist of a number of rotating blades: if the blades are connected to a horizional shaft, the turbine is called a horizional axis wind turbine (HAWT), while if they are connected to a vertical-shaft the machine is called vertical axis wind turbine (VAWT). The most common commercial architectures among wind energy conversion systems are HAWTs, due to their high aerodynamic efficiency. To give a first idea of machine size and power, information about the number of blades, the rated power and the control strategy are also required. The tower height is important as wind speed increases with height above the ground and the rotor diameter gives the area for the available power; the ratio between the rotor diameter D and the hub height H is often approximately one. The rated power is the maximum power allowed for the installed generator and a control system is always present to ensure that generated power is limited during strong winds or gusts.

The machine usually has two or three blades: two-bladed wind turbines are cheaper, but they rotate faster, with negative effects on aerodynamic efficiency; furthermore they appear more flickering to the eyes, whereas three-bladed wind turbines are calmer and therefore less disturbing in the landscape. Also the aerodynamic efficiency depends on the number of blades: it is lower on a two-bladed than on a three-bladed wind turbine. Moreover, for a two-bladed rotor, the connection to the shaft is flexible, as the rotor is mounted on the shaft through a hinge: this is called a teeter mechanism and the effect is that no bending moments are transferred from the rotor to the mechanical shaft. Such a construction is more flexible than the stiff three-bladed rotor and some components can be built lighter and smaller, which thus reduces the price of the entire wind turbine, but the stability of a more flexible rotor must be ensured too. Noise is another parameter that has to be taken into account, in particular downwind turbines are noisier than upstream turbines, since the one-per-revolution tower passage of each blade is perceived as a low frequency noise.

The rotational speed of a wind turbine rotor ranges approximately from $20rpm$ to $70rpm$, instead the rotational speed of the most common generator shafts is approximately $1000rpm$ to $3000rpm$. Therefore a gearbox must be placed between the low speed rotor shaft and the high speed shaft of the generator. In Figure 1.5, a typical layout of a wind turbine is represented, designed by Siemens for offshore applications. The main shaft has two bearings to facilitate a possible replacement of the gearbox during maintenance, but this layout is not the only option: some turbines are equipped with multipole generators, which rotate so slowly that no gearbox is required.

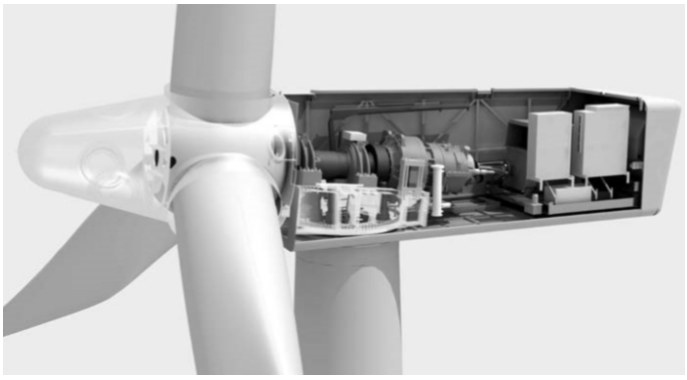

Figure 1.5: *Horiziontal-axis wind turbine (HAWT).*

Ideally a wind turbine rotor should always be perpendicular to the wind to extract more power, for this reason on most wind turbines a wind vane is mounted to measure the direction of the wind. This signal is coupled with a yaw motor, which continuously turns the nacelle into the wind. The rotor has undergone a great development in recent years, in particular in terms of airfoils and materials. On the first modern wind turbine blades, the airfoils used were developed for aircraft, thus not optimized for higher angles of attack that frequently occur in a wind turbine. Nowadays blade manufacturers have started to use airfoils specifically optimized for wind turbines. Different materials have been tested in the construction of the blades, which must be sufficiently strong and stiff, have a high fatigue endurance limit and be cheap. Today most blades are built in composite materials, for example glass fibre reinforced plastic (GFRPs) and carbon fibre reinforced plastics (CFRPs), but other materials such as laminated wood are also used.

1.3 Blade element momentum theory

Methods of various levels of complexity are available to calculate the aerodynamic loads on a wind turbine rotor, starting with the actuator disc model, the well known BEM (Blade Element Momentum), carrying on with lifting line, panel and vortex models and ending with the more complex solution of Navier-Stokes equations.

The present work focuses on BEM method, that is the most common calculation strategy for aerodynamic loads on wind turbines, since it is computationally cheap and very fast. BEM is widely used for initial aerodynamic analysis, conceptual design, loads and stability analysis and controls design; it provides very satisfactory results, in particular if reliable lift and drag coefficients are available as functions of the angle of attack and the Reynolds number. The model was introduced by Glauert (1935) in [4] as a combination of one dimensional momentum theory (1D) and blade element considerations to determine the local loads along the blade span. The following hypotheses are required to the formulation of the model:

- steady state flow;
- frictionless surfaces;
- no radial dependency between each layer of the blade;
- no radial flow across the elements;
- the force from the blades on the flow is constant in each annular element, this means infinite number of blades.

The BEM method highlights to the concept of induced velocity, which is here briefly summarized: the free vortices induce a downwards velocity compoment by the Biot-Savart law at any spanwise position of a 3D wing, as depicted in Figure 1.6. For one vortex filament of strength Γ the induced velocity at point p is:

$$\boldsymbol{W} = \frac{\Gamma}{4\pi} \oint \frac{\boldsymbol{r} \times \boldsymbol{ds}}{r^3} \tag{1.3}$$

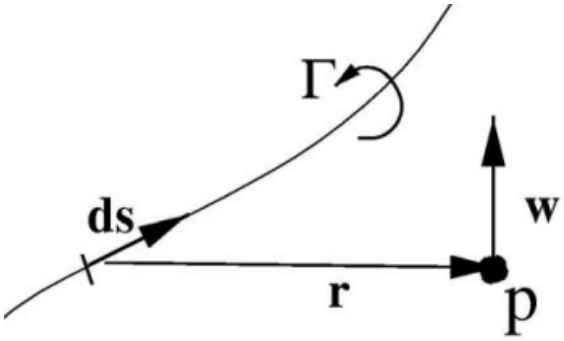

Figure 1.6: *Induced velocity from a vortex line of strength* Γ.

The vortex system causes an axial velocity component opposite to the direction of the wind and a tangential velocity component opposite to the rotation of the rotor blades. The axial induced velocity is specified through the axial induction factor, as aV_0, and the induced tangential velocity in the rotor wake is given by the tangential induction factor, as $2a'\omega r$. Since the flow does not rotate upstream of the rotor, the tangential induced velocity in the rotor plane is approximated as $a'\omega r$. If the induction factors are known, an equivalent 2D approach can be used to calculate axial and tangential velocities as:

$$u = (1 - a)\, V_0 \tag{1.4}$$

$$V_{tang} = (1 + a')\, \omega r \tag{1.5}$$

As explained below, the method is usually subjected to both Glauert correction when the simple momentum theory breaks down and Prandtl's tip loss factor correction to take into account a finite shape aspect ratio. The control volume sketched in Figure 1.7 is used to properly formulate the algorithm, the stream tube is discretized into N annular elements of infinitesimal radial size, dr: the lateral boundaries of these elements consist of streamlines, in other words there is not flow across the lateral elements.

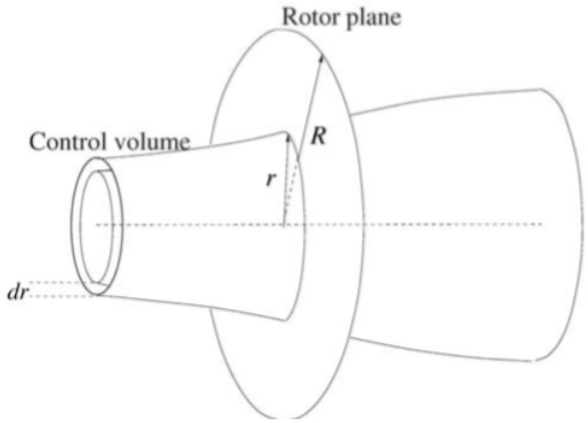

Figure 1.7: *Control volume and annular elements used in the BEM model.*

According to the 1D momentum theory, it was proven in [3] that the pressure distribution along the curved streamlines enclosing the wake does not give an axial force

component; this is assumed for the annular control volume in Figure 1.7. The thrust from the disc on this control volume can thus be found from the integral momentum equation, since the cross-section area of the control volume at the rotor plane is $2\pi r dr$, the infinitesimal thrust becomes:

$$dT = (V_0 - u_1)\, d\dot{m} = 2\pi r \rho u\, (V_0 - u_1)\, dr \tag{1.6}$$

Assuming no rotational components of the wind upstream of the rotor plane, the torque on the annular elements is found using the Euler's equation:

$$dM = \frac{dP}{\omega} = rC_\theta d\dot{m} = 2\pi r^2 \rho u C_\theta dr \tag{1.7}$$

From 1D momentum theory exposed in [3], it was found that $u_1 = (1-2a)V_0$, $u = (1-a)V_0$ and $C_\theta = 2a'\omega r$; using these equations in Equation 1.6 and Equation 1.7, the elementary thrust and the torque can be computed as:

$$dT = 4\pi r \rho V_0^2 a\, (1-a)\, dr \tag{1.8}$$

$$dM = 4\pi r^3 \rho V_0 \omega\, (1-a)\, a' dr \tag{1.9}$$

The left hand side of Equation 1.8 and Equation 1.9 are found from the local inflow conditions around the blade, in particular projections of lift and drag forces along the tangential and normal directions to the rotor plane can be evaluated if the inlet flow angle is known. Angle definition and velocity triangles are depicted in Figure 1.8: it can be seen that the relative velocity, V_{rel}, seen by a blade's layer, is a combination of axial velocity, $(1-a)V_0$, and tangential velocity, $(1+a')\omega r$.

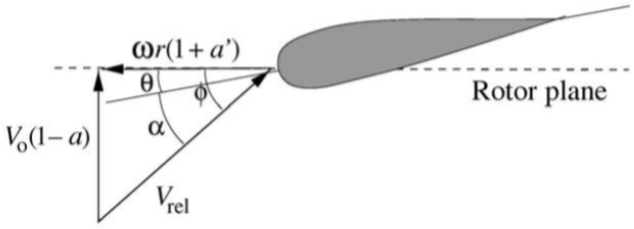

Figure 1.8: *Velocity triangle at the rotor plane.*

Wind turbine blades are characterized by a global pitch angle, θ_p, that is the pitch of the entire blade, and by the local twist at a certain span position, β, so that the local pitch angle, θ, is calculated as $\theta = \theta_p + \beta$. Furthermore, the flow angle, ϕ, is defined as the angle between the plane of rotation and the relative velocity and the angle of attack is evaluated as: $\alpha = \phi - \theta$. Finally, the local flow angle ϕ and the relative velocity V_{rel} are calculated as:

$$\phi = \arctan \frac{(1-a)\, V_0}{(1+a')\, \omega r} \tag{1.10}$$

$$V_{rel} = \frac{V_0\, (1-a)}{\sin \phi} = \frac{\omega r\, (1+a')}{\cos \phi} \tag{1.11}$$

It is also recalled that the lift force, by definition, is perpendicular to the local velocity seen by the 2D airfoil and the drag force is parallel to the same velocity: for wind turbine applications, the just mentioned velocity is the relative velocity, V_{rel}. Equation 1.12 and Equation 1.13 remind the definition of forces:

$$L = \frac{1}{2}\rho V_{rel}^2 c C_l \tag{1.12}$$

$$D = \frac{1}{2}\rho V_{rel}^2 c C_d \tag{1.13}$$

As said before, attention has to be focused on forces normal and tangential to the rotor plane, so lift and drag are projected into these directions as:

$$p_N = L\cos\phi + D\sin\phi \tag{1.14}$$

$$p_T = L\sin\phi - D\cos\phi \tag{1.15}$$

The resulting force, R, is the vector sum of lift and drag, instead p_N and p_T are normal and tangential components of R respectively, as Figure 1.9 shows.

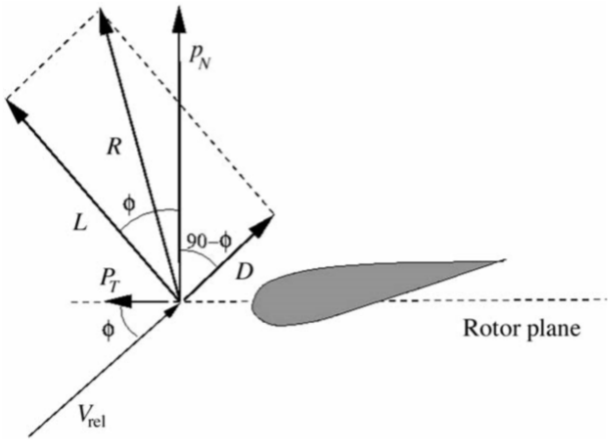

Figure 1.9: *Airfoil loads projection.*

Equation 1.14 and Equation 1.15 are normalized with respect to $0.5\rho V_{rel}^2 c$ yielding:

$$C_n = \frac{p_N}{0.5\rho V_{rel}^2 c} = C_l\cos\phi - C_d\sin\phi \tag{1.16}$$

$$C_t = \frac{p_T}{0.5\rho V_{rel}^2 c} = C_l\sin\phi - C_d\cos\phi \tag{1.17}$$

Since p_N and p_T are forces per unit length, the normal force and the torque contribution on control volume of thickness dr are evaluated as:

$$dT = Bp_N dr \tag{1.18}$$

$$dM = rBp_T dr \tag{1.19}$$

Using Equation 1.16 for p_N and Equation 1.11 for V_{rel}, Equation 1.18 becomes:

$$dT = \frac{1}{2}\rho B \frac{V_0^2 \left(1-a\right)^2}{\sin^2\phi} c C_n r dr \tag{1.20}$$

Similarly, if Equation 1.17 for p_T and Equation 1.11 for V_{rel}, Equation 1.19 becomes:

$$dM = \frac{1}{2}\rho B \frac{V_0 \left(1-a\right)\omega r \left(1+a'\right)}{\sin\phi\cos\phi} c C_t r dr \tag{1.21}$$

Further, the solidity σ is defined as the fraction of the annular area in the control volume which is covered by the blades:

$$\sigma = \frac{cB}{2\pi r} \tag{1.22}$$

If Equation 1.20 and Equation 1.8 are combined together with the definition of solidity, an expression for the axial induction factor a is obtained:

$$a = \left(\frac{4\sin^2\phi}{\sigma C_n} + 1\right)^{-1} \tag{1.23}$$

Likewise, if Equation 1.21 and Equation 1.9 are put together, an expression for tangential induction factor a' is derived:

$$a' = \left(\frac{4\sin\phi\cos\phi}{\sigma C_t} - 1\right)^{-1} \tag{1.24}$$

Finally, the thrust coefficient can be calculated as:

$$C_T = \frac{\left(1-a\right)^2 \sigma C_n}{\sin^2\phi} \tag{1.25}$$

In order to get accurate results, it is necessary to apply two corrections to the algorithm: Prandtl's tip loss factor and Glauert correction. The Prandtl's tip loss factor corrects the assumption of an infinite blade aspect ratio and a finite number of blades, since a two or three bladed rotor is characterized by a different vortex system in the wake. The derivation of tip loss factor F can be found in [4]. The correction factor F is evaluated as:

$$F = \frac{2}{\pi}\arccos\left(e^{-f}\right) \tag{1.26}$$

where f is computed as:

$$f = \frac{B}{2}\frac{R-r}{r\sin\phi} \tag{1.27}$$

According to these correction, Equation 1.23 and Equation 1.24 become:

$$a = \left(\frac{4F\sin^2\phi}{\sigma C_n} + 1\right)^{-1} \tag{1.28}$$

$$a' = \left(\frac{4F\sin\phi\cos\phi}{\sigma C_t} - 1\right)^{-1} \tag{1.29}$$

Finally, Equation 1.28 and Equation 1.29 are the proper equations used in BEM algorithm. The Glauert correction is applied when the axial induction factor becomes greater than approximately 0.4, avoiding non-physical results of 1D momentum theory, as shown in Figure 1.10.

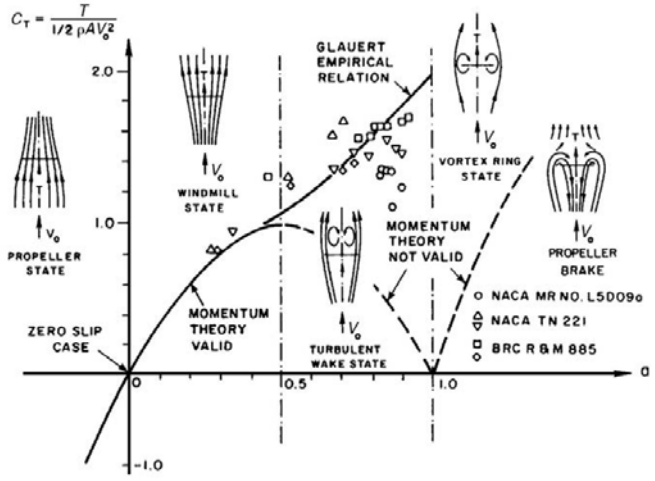

Figure 1.10: *Measured thrust coefficient at the corresponding rotor state.*

Different empirical relationships betweet thrust coefficient and axial induction factor have been derived to best fit the experimental data, some of them are reported in [4] and [5]; the one employed in the present code is explained in [6], where the thrust coefficient is given as:

$$C_T = \frac{8}{9} + \left(4F - \frac{40}{9}\right) a + \left(\frac{50}{9} - 4F\right) a^2 \tag{1.30}$$

or

$$a = \frac{18F - 20 - 3\sqrt{C_T\,(50 - 36F) + 12F\,(3F - 4)}}{36F - 50} \tag{1.31}$$

The correction to axial induction factor has to be applied for $a > 0.4$, that is for $C_T = 0.96$. Finally, the axial induction factor is evaluated as:

$$a = \begin{cases} \left(\frac{4F\sin^2\phi}{\sigma C_n} + 1\right)^{-1}, & \text{if } 0 \leq a < 0.4 \\ \frac{18F - 20 - 3\sqrt{C_T(50-36F) + 12F(3F-4)}}{36F-50}, & \text{if } a \geq 0.4 \end{cases} \tag{1.32}$$

As explained before, BEM algorithm requires a convergence iteration loop, whose results are axial and tangential induction factors that allow to calculate the velocity triangles at each blade's layers, in particular the relative velocity, V_{rel}. Now the tangential and normal load distribution can be avaluated as:

$$p_N = \frac{1}{2}\rho V_{rel}^2 c C_n \tag{1.33}$$

$$p_T = \frac{1}{2}\rho V_{rel}^2 c C_t \tag{1.34}$$

The global parameters for a single blade, such as torque and thrust, are calculated as sum of every blade's contribution:

$$M = \int_{R_{hub}}^{R_{tip}} r p_T dr \tag{1.35}$$

$$T = \int_{R_{hub}}^{R_{tip}} p_N dr \tag{1.36}$$

that is solved using a trapezoidal method in the code. Finally, the mechanical power for the whole wind turbine is:

$$P = BM\omega \tag{1.37}$$

All necessary equation for BEM model have been derived and the algorithm can be summarized as the steps below. These steps have to be applied at each layer of the blade, thus the solution in terms of aerodynamic loads is given at each radius.

1. Initialize induction factors, $a = a' = 0$;
2. Compute the flow angle using Equation 1.10;
3. Compute Prandtl's correction factor using Equation 1.27 and Equation 1.26;
4. Compute the local angle of attack as $\alpha = \phi - \theta$;
5. Read lift and drag coefficients from database;
6. Compute C_n and C_t from Equation 1.16 and Equation 1.17;
7. Calculate new induction factors from Equation 1.32 and Equation 1.29;
8. If a and a' changes more than a certain tolerance, go to step 2 or else finish;
9. Compute local and global loads on the blade segment using Equation 1.33 to Equation 1.36;
10. Calculate mechnical power using Equation 1.37.

- II -

Steady BEM validation

The purposes of the following chapter are the development and the validation of Reynolds tables of polars to be coupled with an existing BEM code, implemented by the COMETES research group [1].

2.1 Polar tables

Polars calculation deeply affect predictions of a BEM method, as said in [3]; shape of profile, angle of attack, Mach and Reynolds number should be taken into account at each blade element layer to a proper choice of lift and drag coefficients. Wind turbine blades are long and slender structures where spanwise velocity component is lower than the streamwise one, therefore in many aerodynamic models it is assumed that the flow at a given radial position is two dimensional and that 2D aerofoil data can thus be applied. In wind turbine applications, effects of compressibility are ignored because of the low speed of the air, so dependency of polar on Mach number may be neglected in this work, as it is lower than 0.3. A brief review of lift, drag and moment coefficient definitions is given by Figure 2.1 and Equation 2.1 to Equation 2.3:

$$C_l = \frac{L}{0.5\rho V_\infty^2 c} = f\left(\alpha, Re, airfoil\right) \tag{2.1}$$

$$C_d = \frac{D}{0.5\rho V_\infty^2 c} = f\left(\alpha, Re, airfoil\right) \tag{2.2}$$

$$C_m = \frac{M}{0.5\rho V_\infty^2 c^2} = f\left(\alpha, Re, airfoil\right) \tag{2.3}$$

2.1.1 Panel codes

First step is the creation of a large polar database of S809, S812, S813 and S814 airfoils, according to different angles of attack (step size 0.5°) and Reynolds number between 200.000 and 2.000.000 (step size 200.000). This database development is a stand alone routine that provides data of lift and drag coefficients; hence BEM algorithm will call polar airfoils table when needed. As CFD computation would be excessively time consuming, two different panel codes have been used to evaluate lift and drag coefficients, $xFoil$ and

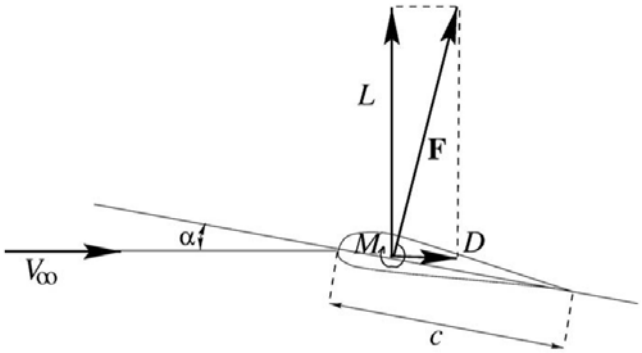

Figure 2.1: *Definition of lift and drag.*

rFoil, spending less that five minutes using a common laptop. A short review of the main differences between the two panel codes is here summarized: *xFoil* evaluates polar diagrams for a greater number of angles of attack, but with less precision; on the other side *rFoil*, an improved version of *xFoil*, is endowed with more accuracy, in particular in the stall region, but usually stops the calculation for smaller angles of attack at low Reynolds and suffers from instability problems. Some polars are represented from Figure 2.2 to Figure 2.5 according to different Reynolds numbers and airfoils. Drag coefficient evaluation is very similar according to both panel codes, as happened for the lift coefficient in the linear region of attached flow. On the other side, from the beginning of the stall region, lift coefficient is overestimated by *xFoil*, as seen from Figure 2.2 to Figure 2.4.

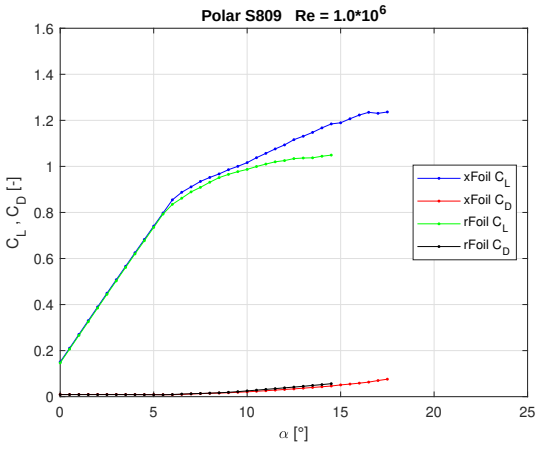

Figure 2.2: *Polar comparison S809 airfoil.*

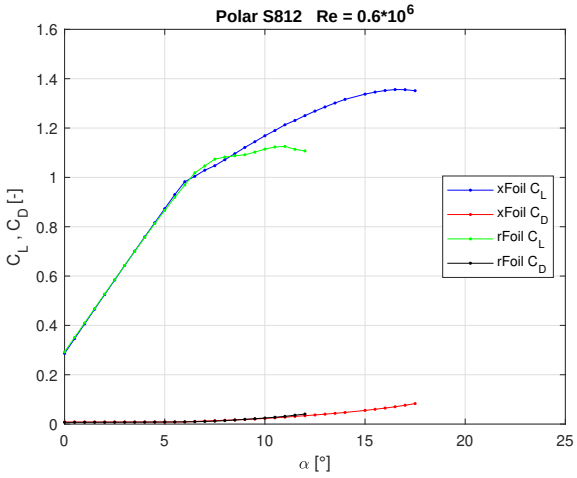

Figure 2.3: *Polar comparison S812 airfoil.*

As panel codes predictions are deeply affected by the accuracy and the number of points used to reproduce the airfoil, a good choice is to carry out a parametrization of the airfoil with Bézier curves, instead of using a little set of points from [7]. Airfoils are cutted off at 99.5% of the chord to avoid convergence failure in the trailing edge zone. Thanks to an accurate revision of the obtained results, polar prediction of *xFoil* is considered reliable only for a maximum of 1.5° after the angle of stall α^*, thus the polar data acquisition is stopped at a fixed angle α_{lim} that fulfills the following relationships:

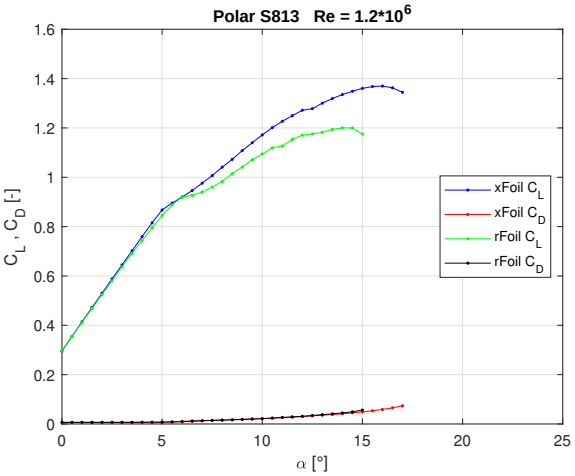

Figure 2.4: *Polar comparison S813 airfoil.*

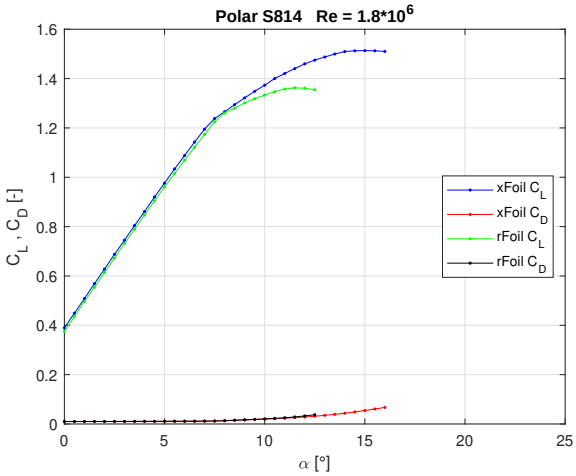

Figure 2.5: *Polar comparison S814 airfoil.*

$$\alpha_{lim} = \alpha^* + 1.5^\circ \tag{2.4}$$

where

$$C_l(\alpha^*) = C_{l,max} \tag{2.5}$$

The maximum value of lift coefficient points out the beginning of stall phenomena: sometimes panel codes, as $xFoil$, are able to predict more data after stall, but with bigger uncertainty due to the presence of unpredictable unsteady events. On the other side, every data of $rFoil$ polar is considered reliable, as $rFoil$ is a more accurate version than $xFoil$, especially in the stall region.

2.1.2 Extrapolation

Panel codes provide lift and drag coefficients in a small range of angles of attack, however, wind turbines are usually characterized by great angles of attack. Thus, a procedure to extrapolate airfoil polars is required in order to obtain data for the whole range of angles of attack: the present study compares the lift and drag coefficients extrapolation using flat plate theory and Viterna method. Both methods have been implemented thanks to a Python routine, $Airfoil Prep.py$, presented in [8] and integrated in the code to obtain the extrapolated polar tables from the diagrams obtained by the panel code, characterized by a small range of angles of attack. According to Viterna, extrapolated polars are obtained from Equation 2.6 and Equation 2.7:

$$C_l = \begin{cases} x\text{-}or\text{-}rFoil, & if\ 0 \leq \alpha \leq \bar{\alpha} \\ A_1 \sin 2\alpha + A_2 \frac{\cos^2 \alpha}{\sin \alpha}, & otherwise \end{cases} \tag{2.6}$$

$$C_d = \begin{cases} x\text{-}or\text{-}rFoil, & if\ 0 \leq \alpha \leq \bar{\alpha} \\ B_1 \sin 2\alpha + B_2 \cos \alpha, & otherwise \end{cases} \tag{2.7}$$

where $\bar{\alpha}$ is the starting extrapolation angle, A_1, A_2, B_1 and B_2 are given by:

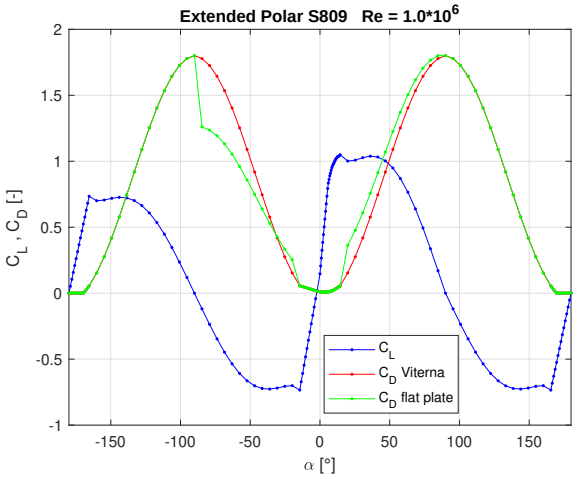

Figure 2.6: *Extended polar comparison.*

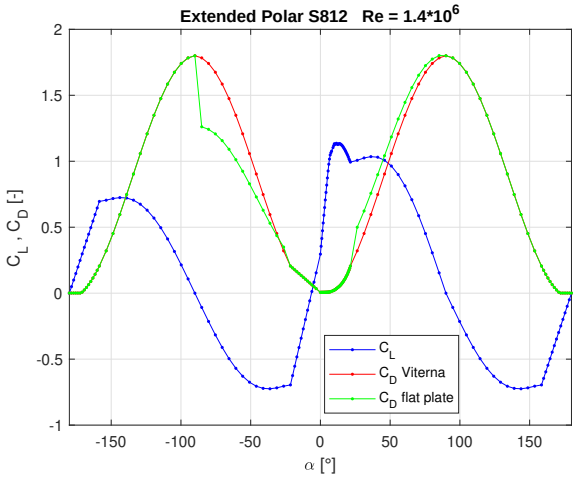

Figure 2.7: *Extended polar comparison.*

$$A_1 = \frac{C_{d,max}}{2} \tag{2.8}$$

$$A_2 = \left(C_l\left(\bar{\alpha}\right) - C_{d,max}\sin\bar{\alpha}\cos\bar{\alpha}\right)\frac{\sin\bar{\alpha}}{\cos^2\bar{\alpha}} \tag{2.9}$$

$$B_1 = C_{d,max} \tag{2.10}$$

$$B_2 = \frac{C_d\left(\bar{\alpha}\right) - C_{d,max}\sin^2\bar{\alpha}}{\cos\bar{\alpha}} \tag{2.11}$$

Maximum drag coefficient is required as an input to the routine, reasonably assumed as:

$$C_{d,max} = 1.8 \tag{2.12}$$

In extrapolating data for $\alpha < 0°$ and $\alpha > 90°$ the calculated values are reflected. On the other hand, flat plate theory is used for all angles of attack $\alpha_{lim} < \alpha < 90°$ to predict drag coefficient as follow:

$$C_d = C_l \tan\alpha \tag{2.13}$$

Both formulations give the same lift coefficient, while differences affect the drag coefficient, as shown in Figure 2.6 and Figure 2.7. Only a subsequent validation of the BEM code coupled with Reynolds polar tables allows to point out which formulation is more appropriate among Viterna method and flat plate theory.

2.2 Validation

The second step is the development and the aerodynamic validation of a routine inside the BEM code used to interpolate lift and drag coefficients, not only according to the

angle of attack, but also according to the Reynolds number at each blade's layers and iteration, thanks to the database of airfoil polar data. The flow chart of interpolation can be summarized by the following steps to be applied at each blade's layer. The routine inside the code starts from the actual value of angle of attack, α, and Reynolds number, Re:

1. Identify Re_{inf} and Re_{sup}, lower and upper boundaries of Re;
2. Interpolate lift and drag coefficient on α at Re_{inf}, using extended polar tables at Re_{inf};
3. Interpolate lift and drag coefficient on α at Re_{sup}, using extended polar tables at Re_{sup};
4. Interpolate lift and drag coefficient on Re, using values from steps 2 and 3.

During the validation process it was clear that some scale factor was needed to correct the generated power, in order to achieve a good matching with experimental data. Thanks to some background knowledge of the COMETES research group from the University of Padova, sources of uncertainty reveal to originate from panel codes: penalty factors for $xFoil$ and $rFoil$ have been defined, respectively. Penalty factors can be considered to account for phenomena not treated in the BEM method, such as the presence of the tower, not homogeneous incoming wind, different wind direction during experimental testing, dependency of polar diagrams on Reynolds number and so on. Finally, in order to validate lift and drag coefficients calculation routine, two horizontal axis wind turbine have been chosen as test cases: AOC 15/50 and NREL Phase VI.

2.2.1 AOC 15/50

The AOC 15/50 wind turbine is located at the National Wind Technology Center, in Colorado (USA), at an elevation of $1830m$ above *s.l.*. Technical data of the turbine are summarized in Table 2.1 and experimental data of the steady power curve, used to validate the code, are available in [9].

airfoil - hub	S814	rotational speed $[rpm]$	65
airfoil - mid	S812	cut-in speed $[m/s]$	4.9
airfoil - tip	S813	cut-off speed $[m/s]$	22.3
number of blades	3	rated power $[kW]$	50
rotor diameter $[m]$	15	power regulation	stall
tower heigh $[m]$	24.4	design wind speed $[m/s]$	12
pitch setting $[^\circ]$	1.54	control type	fixed pitch

Table 2.1: *AOC 15/50 technical data.*

The existing BEM code [1] computes the generated power using only one set of polars, evaluated for a single Reynolds number of 1.3 10^6 and 1.0 10^6, in case of $xFoil$ or $rFoil$ polars are used respectively. Thus a comparison between previous BEM code version

Figure 2.8: *AOC 15/50 test turbine.*

[1] and the current one, characterized by Reynolds interpolation routine, has been carried out. Both calculations have been initialized as summarized in Table 2.2; for the old version penalty parameters of 1.30 for $xFoil$ and 1.14 for $rFoil$ were adopted.

number of layers	100
tolerance	10^{-5}
maximum iterations	100
relaxation parameter	0.35
generator efficiency	0.860
$rFoil$ penalty	0.98
$xFoil$ penalty	1.05

Table 2.2: *BEM code initialization.*

In order to obtain a stable convergence and to avoid a possibile numerical failure, an under-relaxation technique has been applied to the calculation of induction factors during the iteration process:

$$a_{i+1} = a_i\lambda + (1-\lambda)\, a_i \tag{2.14}$$

$$a'_{i+1} = a'_i\lambda + (1-\lambda)\, a'_i \tag{2.15}$$

where a_{i+1} and a'_{i+1} represent the new values of induction factors, a_i and a'_i the previous ones and λ the relaxation parameter.

The previous BEM version [1] used the default suggested density by [3], $\rho = 1.225$ kg/m^3, instead of a more appropriate value, $\rho = 1.012$ kg/m^3, exposed in [9]; hence available results from previous code have been corrected with a proper scale factor to be referred to the same conditions. Furthermore, to properly compare old and new results, the same penalty factor for $xFoil$ and $rFoil$ has to be applied, so the penalty factors of

the new version of the code have been taken into account. The scaling procedure allows to compare power results scaled by the same factor in order to emphasize the advantages of the Reynolds database interpolation. Thanks to the proposed changes to the BEM code, penalty factors have been reduced to 1.05 and 0.98 for $xFoil$ and $rFoil$ respectively.

Figure 2.9 represents the results obtained with flat plate theory, using both $xFoil$ and $rFoil$ polars. Not only the general trend is well reproduced, but an optimum matching between predicted values and measurements is achieved, in particular $rFoil$ routine calculation manages to capture stall conditions of the blades. Low speed wind operating conditions involve inertial and starting phenomena of the turbine, not taken into consideration by the BEM model, so that the power output is overestimated, but without negative effect on the general accuracy of the model, since the low wind speed zone is characterized by low power production. At medium-low wind speed, both panel codes give the same power results because, as seen before, lift and drag coefficients stay in the same linear trend in the polar plots. Results with Viterna method of extrapolation are shown in Figure 2.10, at medium low wind speed a good prediction is achieved, but at high speed the code does not succeed in reproducing physical phenomena occurring during stall behaviour.

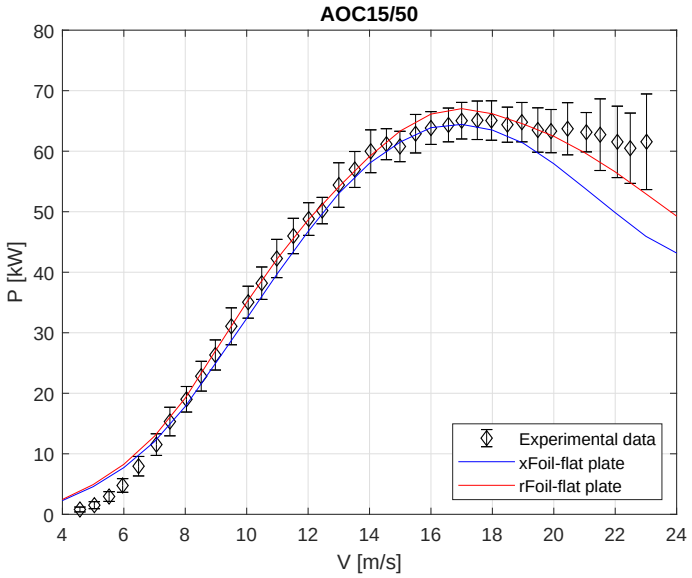

Figure 2.9: *Power curve, current BEM code, flat plate theory.*

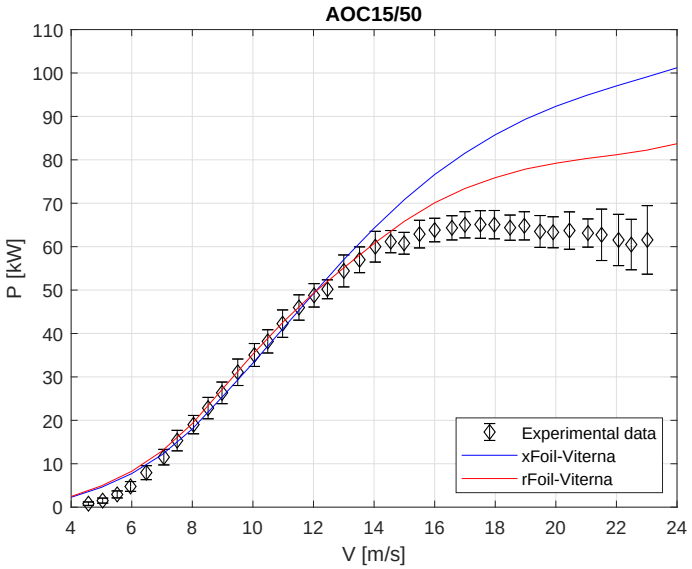

Figure 2.10: *Power curve, current BEM code, Viterna theory.*

According to corrections of density and penalty factors, a comparison between the previous and the current BEM codes is reported in Figure 2.11 and Figure 2.12: improvements appear clearly, especially with $rFoil$ code in the stall region. During the validation process, it has been pointed out that results are deeply affected both by accuracy in polar evaluation and by polar extrapolation method; in particular $rFoil$ appears more reliable than $xFoil$ and flat plate theory reveals a better matching with experimental data than Viterna method. Positive effects in terms of accuracy, maximum power prediction and stall behaviour has been found.

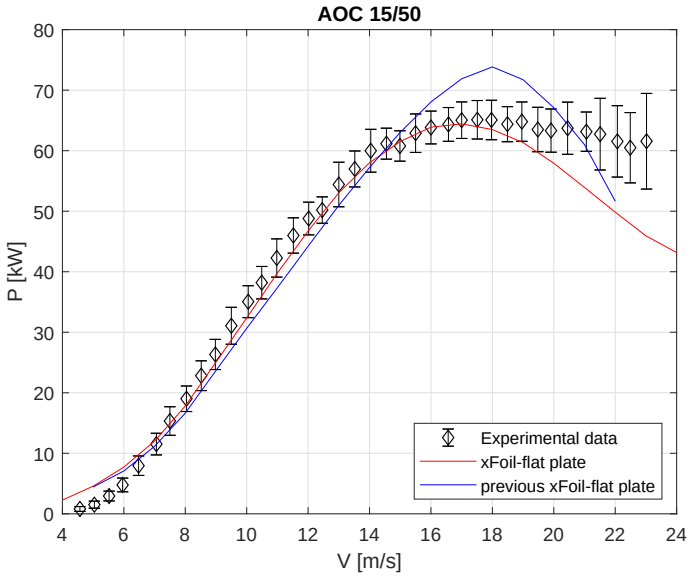

Figure 2.11: *Power curve, flat plate theory, comparison between current and previous BEM codes.*

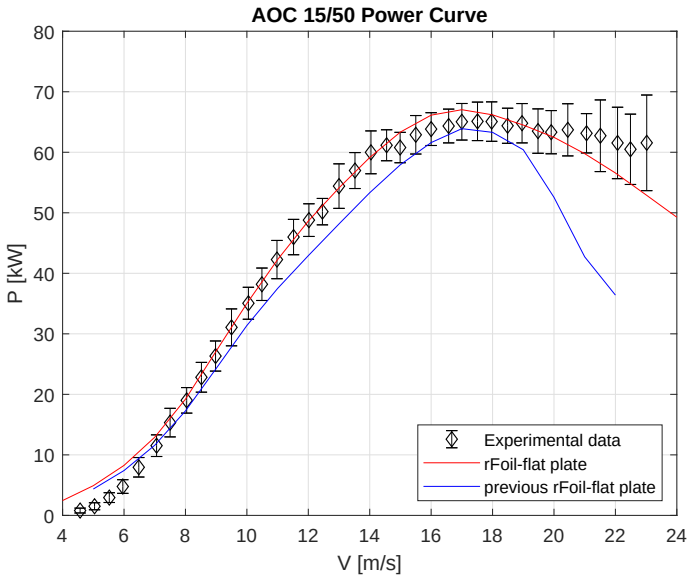

Figure 2.12: *Power curve, flat plate theory, comparison between current and previous BEM codes.*

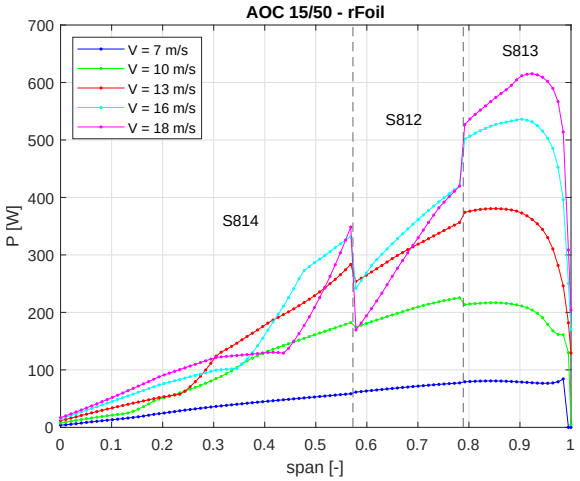

Figure 2.13: *Spanwise power.*

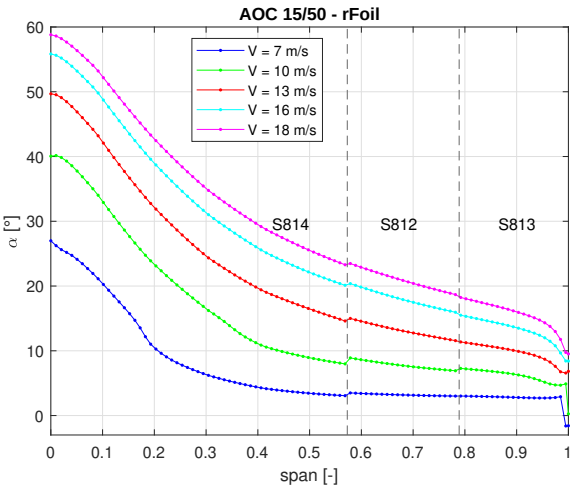

Figure 2.14: *Spanwise angle of attack.*

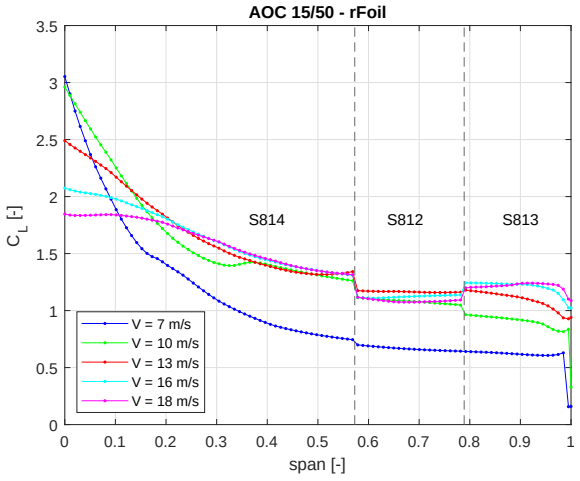

Figure 2.15: *Spanwise lift coefficient.*

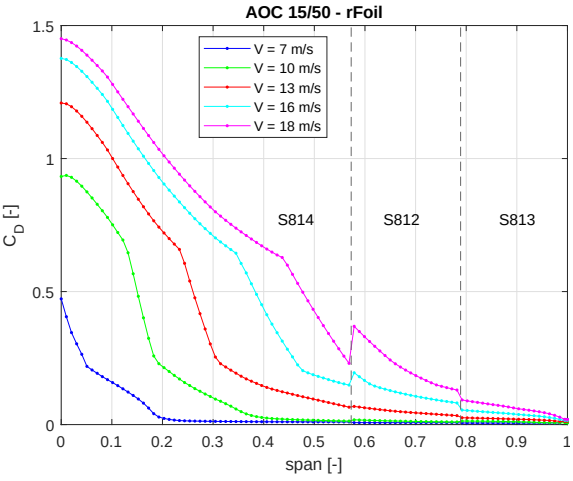

Figure 2.16: *Spanwise drag coefficient.*

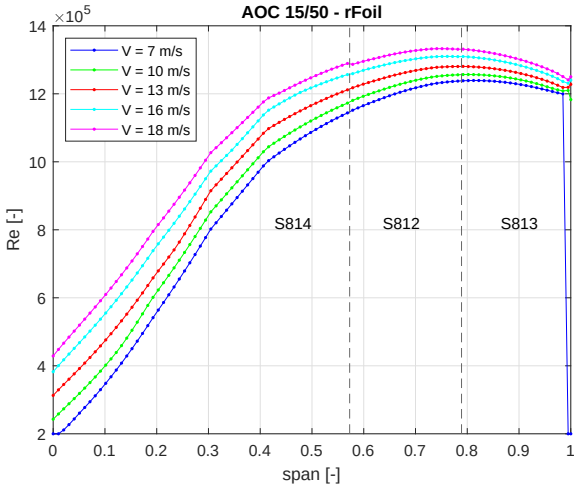

Figure 2.17: *Spanwise Reynolds number.*

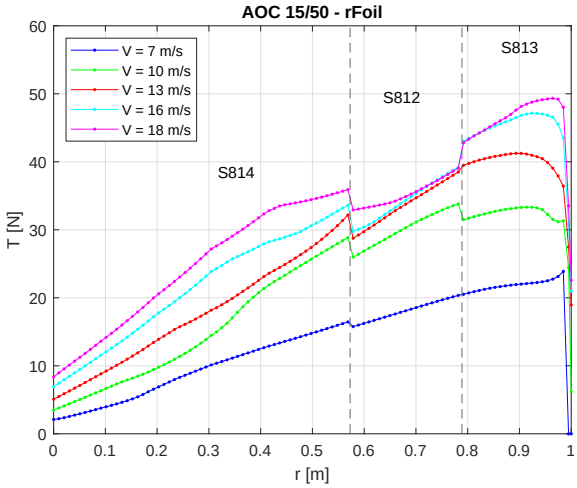

Figure 2.18: *Spanwise thrust.*

A spanwise analysis of power, angles of attack, lift and drag coefficients, Reynolds number and thrust has been carried out in order to understand the involved phenomena at different wind speeds; results discussed as follows refer to $rFoil$ polars, extended using flat plate theory. Figure 2.13 shows the spanwise power trend of each blade layer at several wind speeds; as expected, power production grows up from hub to tip and increases with wind velocity. Especially at high wind speed, a marked step at radii $4.49m$ and $5.99m$ appears, due to the changing between S812 and S813 airfoil; as in the previous code [1], no transition zone between the airfoils is taken into account: these abrupt variations will take place, but with negligible effects on the global power output of the machine. A real blade is characterized by with a transition zone between the airfoils for manufacturability reasons.

As presented in Figure 2.14, high values of angles of attack are involved. Figure 2.15 and Figure 2.16 represent lift and drag coefficients, whereas Reynolds number and thrust are shown in Figure 2.17 and Figure 2.18. Furthermore, at tip sections, the vortex system in the wake is different from the one of a rotor with an infinite number of blades: Prandtl's tip loss factor is used to correct this assumption, but some abrupt variations can be seen at the tip layers, due to the highly 3D aerodynamics in that region.

2.2.2 NREL Phase VI

Experimental data of NREL Phase VI are available in [10] and main technical data are summarized in Table 2.3. A good response of the validation process for another wind turbine further confirms precision and accuracy of the current version of the code.

airfoil	S809	pitch setting [°]	4.815
number of blades	2	rotational speed $[rpm]$	71.63
rotor diameter $[m]$	5.029	rated power $[kW]$	19.80
tower heigh $[m]$	12.20	power regulation	stall

Table 2.3: *NREL Phase VI technical data.*

The BEM code has been initialized using data summarized in Table 2.4; only the generator efficiency of 0.78 is present in [10], but no data about mechanical efficiency at low speed shaft is available, so it is reasonable to assume an efficiency value of 0.847 due to a drive coupling and two bearings (single efficiency of 0.946). The same panel code penalty factor of 0.98 in case of $rFoil$ has been chosen in order to maintain a general validity of the correction; even more so, $rFoil$ code reveals its relevancy to be coupled with the BEM algorithm. On the other hand, a penalty value of 1.30 ensures a good agreement between experimental data and predicted power by $xFoil$ code. The importance to start extrapolating polars from a maximum of 1.5° after the maximum lift coefficient, in case of $xFoil$ only, has also been pointed out ensuring accurate results.

number of layers	100
tolerance	10^{-5}
maximum iterations	100
relaxation parameter	0.35
generator efficiency	0.847
$rFoil$ penalty	0.98
$xFoil$ penalty	1.30

Table 2.4: *BEM code initialization.*

Figure 2.19: *NREL Phase VI test turbine.*

Results obtained with flat plate theory manage to well reproduce the output torque, as it can be seen in the power curve in Figure 2.20. A good matching between calculated results and experimental data have been carried out using $rFoil$ code, but also $xFoil$ well represents the general trend of the curve in terms of maximum power prediction. At high wind speeds, turbine operating conditions are characterized by stall: even if BEM prediction with $rFoil$ is less accurate than $xFoil$, it does not give any disadvantages,

since at wind speeds up to the maximum power, a good prediction is more important to validate the code than that one in stall region. For these reasons, the improved version of the BEM code, coupled with Reynolds table interpolation from $rFoil$ data, is considered to be validated for NREL Phase VI wind turbine.

As observed also for AOC 15/50, using Viterna extrapolation method, as shown in Figure 2.21, is not a good choice because the general behaviour of the wind turbine does not fit experimental data at medium and high velocities and the general trend is not reproduced; above $10m/s$ the power output has been predicted correctly by the code using $rFoil$ polar diagrams.

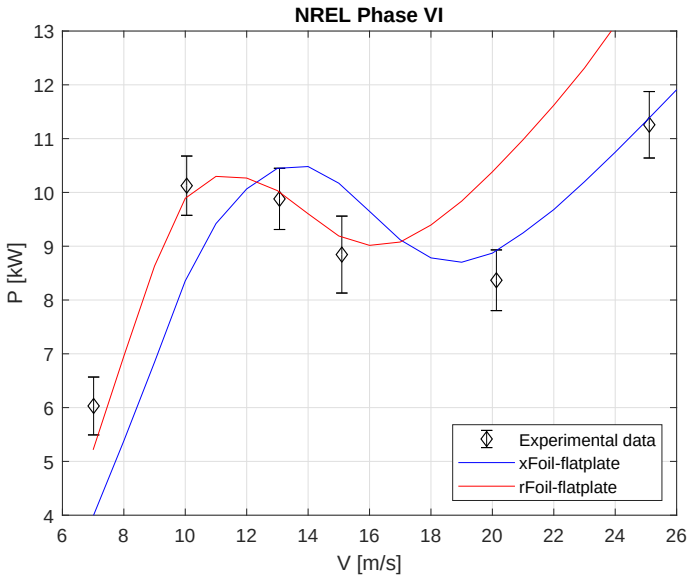

Figure 2.20: *Power curve.*

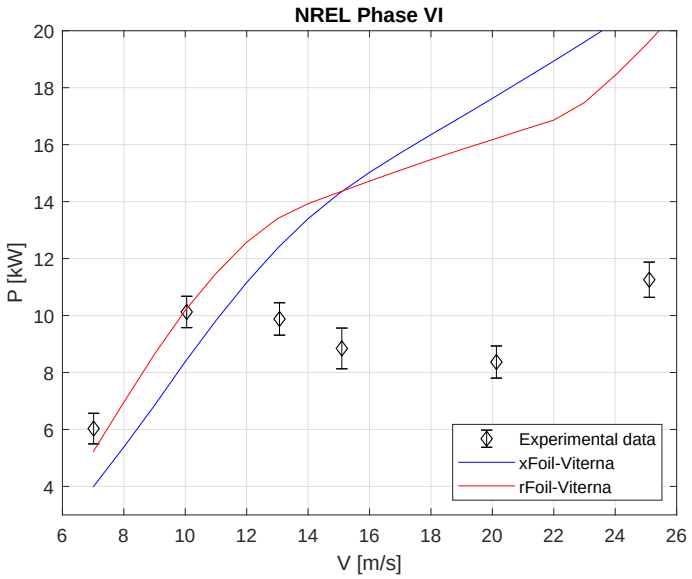

Figure 2.21: *Power curve.*

An analysis of spanwise quantities, such as power, angle of attack, lift and drag coefficients, Reynolds number and thrust are presented as follows referring to flat plate theory

and *rFoil* code. Focusing on the tip region of the curves at $8m/s$, $12m/s$ and $16m/s$ in Figure 2.22, power production grows up, but always for smaller span regions, since the stall advances from hub to tip, as it can be seen in Figure 2.25 for the same velocities. In [11] the stall development has been predicted at the same velocity by a CFD computation. In the hub region, the power curve grows up gradually along the span for increasing wind speeds; at $24m/s$, the slope of the curve is opposed to that one at $8m/s$: lift over drag ratio coefficient is low for each span at high wind speeds, so the layers characterized by greater chord give more contribution to power production, *i.e.* hub layers. Therefore, the post-stall power peak in Figure 2.20 is linked to this phenomenon. Finally, the trends of angle of attack, Reynolds number and wind thrust are represented in Figure 2.26 and Figure 2.27. Each spanwise curve is related to each other, so many considerations can be carried out focusing on these plots: for example, at 74% span and in particular for high wind speed, the lift coefficient goes down with the same jump that is shown in the radial power. At the end of the validation process, the importance of using proper lift and drag coefficients and also their extrapolated values underline the influence on accuracy of BEM prediction and spanwise distribution of the main flow variables.

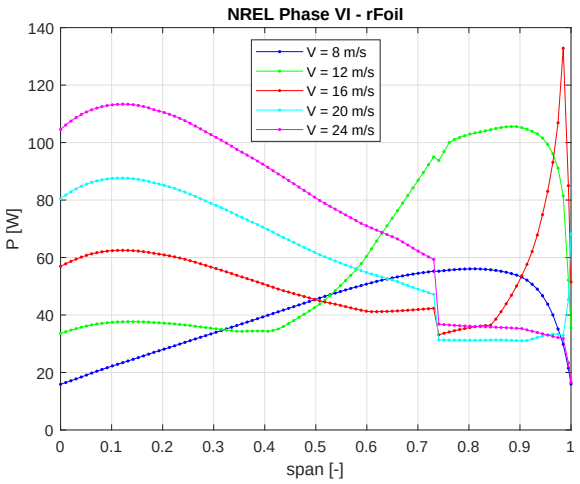

Figure 2.22: *Spanwise power.*

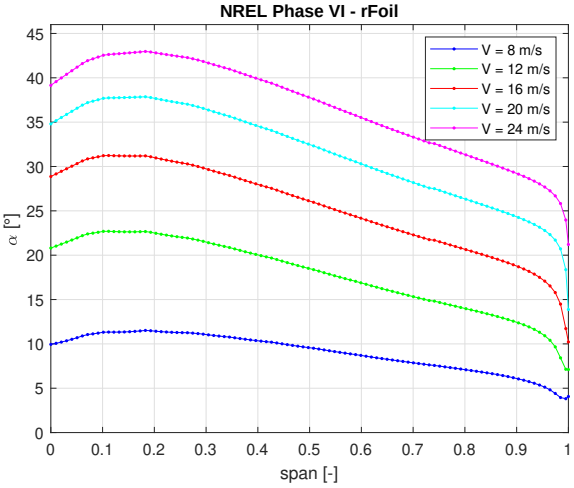

Figure 2.23: *Spanwise angle of attack.*

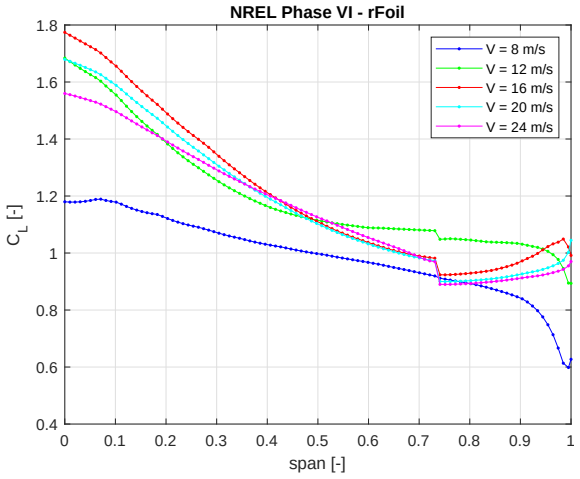

Figure 2.24: *Spanwise lift coefficient.*

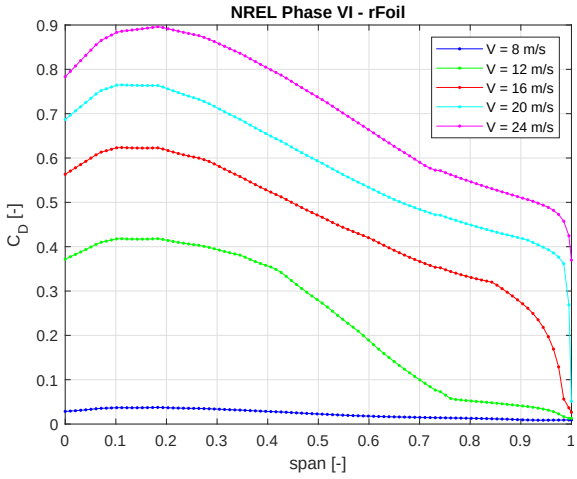

Figure 2.25: *Spanwise drag coefficient.*

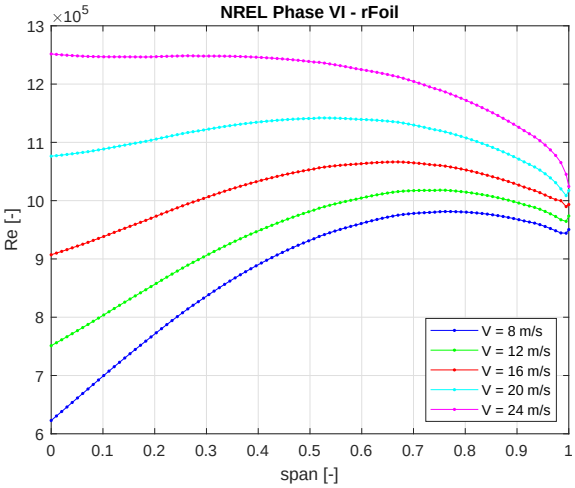

Figure 2.26: *Spanwise Reynolds number.*

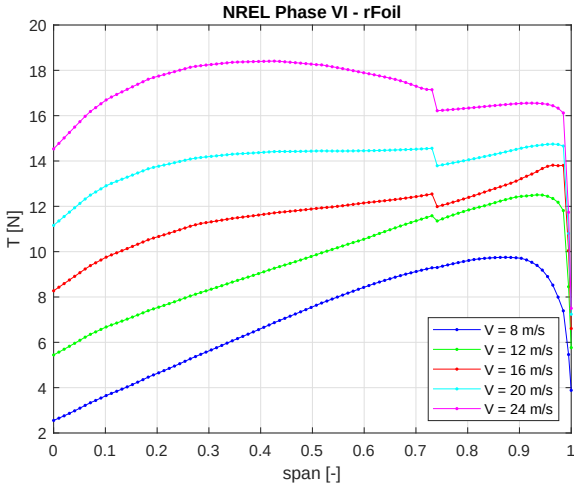

Figure 2.27: *Spanwise thrust.*

Finally, the upgrades to the previous BEM code [1], which have been presented in this section, are summarized as follows:

- limitation of $xFoil$ polar only for a maximum of 1.5° after the stall;
- creation of a wide dataset of polar tables according to Reynolds numbers from 200.000 to 2.000.000;
- development of an interpolation routine inside the BEM code to provide the correct lift and drag coefficients at each layer according to the Reynolds number.

2.3 Sensitivity analysis

Very fast computations is one of the main benefits of a BEM code. Both high and low fidelity algorithms, such as CFD and BEM, need a discretization of computational domain: in case of BEM codes, the blade is divided into several layers onto which the algorithm is applied as a stand alone routine without any consideration about the radial position.

A sensitivity analysis is necessary in order to decide how many sections are needed and to understand the influence of the number of layers on the final results. AOC 15/50 and NREL Phase VI horizontal axis wind turbine have been used again as test cases, the algorithm has been run for a minimum of 10 to a maximum of 300 layers, with a step size of 10 layers between two following attempts. A coherent metric has been found of in order to judge the quality of obtained results with a single parameter, the so called distance function, dsq, which is evaluated as:

$$dsq = \sqrt{\max_{i=1,\dots,n} \left(P_{exper} - P_{BEM}\right)_i^2} \tag{2.16}$$

where n is the number of experimental data and P_{BEM} is a linear interpolation of the power calculated by BEM method, exactly at the same velocity of experimental data.

As expected, both distance functions present an asymptotic trend, clearly evident in Figure 2.28 and Figure 2.29; in case of NREL Phase VI, the distance function presents a serrated behaviour, that seems to reduce its sharpness with the number of layers.

A proper number of 100 layers has been chosen for both wind turbines in order to achieve an accurate estimation of power curve, without an excessive time consumption. In particular, for AOC 15/50 the changing in *dsq* value is about 6.9% between 100 and 300 layers, but Figure 2.30 shows that the differences in power curve appear very slight, even if the percentage value in *dsq* is not inferior to 3%, so not negligible from an engineering point of view. In case of NREL Phase VI the variation in *dsq* between 100 and 300 layers is about 1.3%, and Figure 2.31 justifies the choice of 100 layers. Finally, it is observed that the increasing number of layers produces a global increasing of power curve.

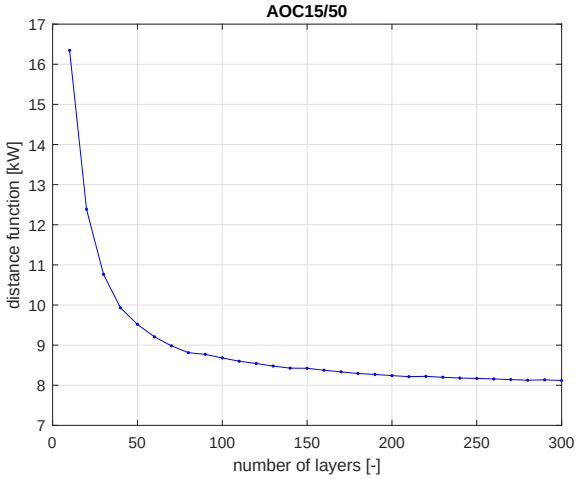

Figure 2.28: *Sensitivity analysis for AOC 15/50.*

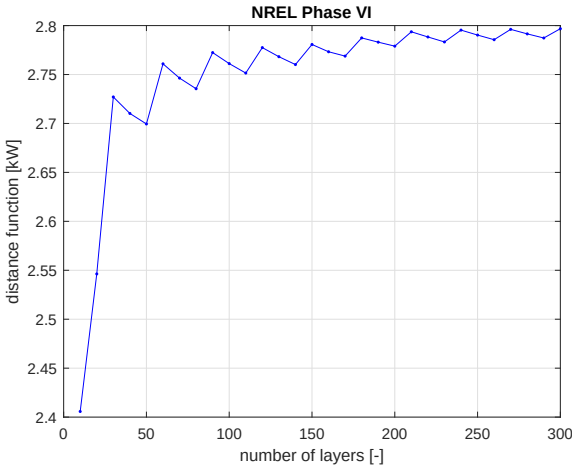

Figure 2.29: *Sensitivity analysis for NREL Phase VI.*

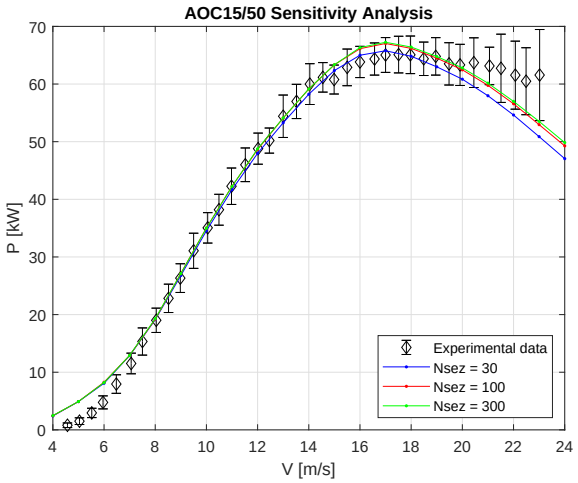

Figure 2.30: *Comparison between different layers for AOC 15/50.*

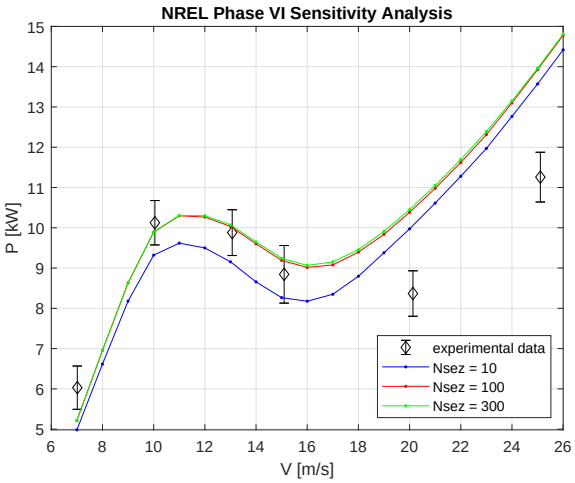

Figure 2.31: *Comparison between different layers for NREL Phase VI.*

- III -

Unsteady BEM model

The purposes of the following chapter are to explain the structure of an unsteady BEM model (UBEM) and to propose a flow chart of the code, focusing on different routines which compose the algorithm.

3.1 UBEM structure

An unsteady BEM code, UBEM, has been studied and developed in this thesis referring to Hansen [3], [5]; the unsteady version of the code appears as the natural update of the steady BEM algorithm, described in Chapter 1 and improved in Chapter 2. A lot of other phenomena are not taken into account in the steady BEM:

- the rotor is not always perpedicular to the incoming wind, so that yaw, tilt and cone angles may appear;
- the wind seen can change in time and direction due to atmospheric turbulence, wind shear and presence of the tower;
- more appropriate and complex models should be considered for the aerodynamic loads on rotating blades, *i.e.* dynamic stall and dynamic inflow;
- the velocity of the vibrating blades changes the relative velocity and thus the aerodynamic loads: a complete structural model of the machine should be coupled with the unsteady BEM method for an aeroelastic computation of the wind turbine.

It is now clear that a more accurate analysis of a wind turbine should take into account these phoenomena, since they are characteristics of the unsteady flow. This work focuses in particular on the development of the general structure of an unsteady code, on the implementation of a yaw routine and of a dynamic stall model. Attention has not been focused only on the computer implementation of the mathematical models, but also on the validation and on a critical analysis of the physical phoenomena occuring during the simulations. About that, the NREL Phase VI horizontal axis wind turbine has been chosen as test case, thanks to its wider experimental dataset available in [10].

The main contributions to realize the unsteady BEM code are represented by: yaw, dynamic stall and dynamic inflow models, each one introduces some time dependent corrections to the basic steady algorithm. In particular yaw and dynamic inflow models

correct at each iteration the value of axial induction factor and induced velocity, respectively; dynamic stall gives a new prediction of the lift coefficient, according to a more complex theory referring to the unsteady aerodynamic loads on an airfoil.

In Figure 3.1 all the velocity components that contribute to the calculation of relative velocity seen by a blade's layer are represented. Equation 3.1 is used in the unsteady BEM code to evaluate the relative velocity and it is posed in the most general form because it also takes into account the blade's section velocity, $\boldsymbol{V_{blade}}$, in case of an aeroelastic computation:

$$\boldsymbol{V_{rel}} = \boldsymbol{V_0} + \boldsymbol{V_{rot}} + \boldsymbol{W} - \boldsymbol{V_{blade}} \tag{3.1}$$

that can be expressed referring to components in layer plane (yz in Figure 3.1) as:

$$\begin{pmatrix} V_{rel,y} \\ V_{rel,z} \end{pmatrix} = \begin{pmatrix} V_{0,y} \\ V_{0,z} \end{pmatrix} + \begin{pmatrix} -\omega r \cos\theta_{cone} \\ 0 \end{pmatrix} + \begin{pmatrix} W_y \\ W_z \end{pmatrix} - \begin{pmatrix} V_{blade,y} \\ V_{blade,z} \end{pmatrix} \tag{3.2}$$

In Equation 3.2 the cone angle takes into account that the blade direction is not always orthogonal the shaft direction, further details are explained in [3]. The definition of induced velocity, $\boldsymbol{W}$, is given by Equation 1.3 and the expressions for the axial and tangential components are reminded as a function of induction factors:

$$W_y = -a'\omega r \tag{3.3}$$

$$W_z = -aV_0 \tag{3.4}$$

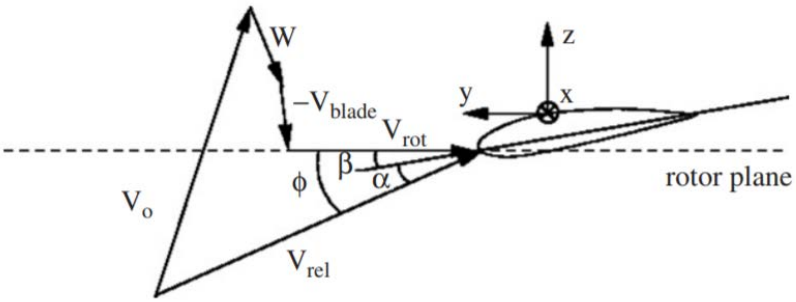

Figure 3.1: *Velocity components seen by a blade's layers.*

The structure of the unsteady BEM code has been organized as represented by the flow chart in Figure 3.2. At the beginning of the simulation the basic inputs are initialized:

- geometry (radius, chord, twist, number of blades);
- operating conditions (angular velocity, pitch and yaw angles, generator efficiency);
- environmental parameters (air density, kinematic viscosity);
- simulation parameters (number of iterations and layers, panel codes penalty, convergence tolerance, time step, relaxation parameter).

As a convention, the analysis starts at time $t_1 = 0s$, that correspons to zero azimuth position for blade number 1 at 12 o'clock, then the azimuth angles associated to the other blades are shifted forward of an angle of $360°/B$. Then the code enter the blade loop that selects which blade has to be analyzed. After that, the time step and the blade are fixed, so the classical BEM loop is applied to each layer, until convergence or maximum number of iterations is reached. So the steady BEM still represents the routine that allows to obtain the axial and tangential induction factors, but yaw, dynamic stall and dynamic inflow models are coupled in the convergence loop.

The general structure of the unsteady BEM code has been developed, in particular this work focuses on implementation an validation of yaw and dynamic stall models; dynamic inflow model will be a future update of the code. Some of the main scripts, functions and other files implemented for the unsteady analysis are:

1. *Input_data_NREL.txt*: basic geometrical inputs;
2. *input_Parameters.m*: inputs to initialize simulation;
3. *main_UBEM.m*: main of UBEM structure;
4. *BEMR.m*: blade element momentum routine;
5. *model_LiftDragCoefficient.m*: lift and drag coefficients calculation;
6. *model_Yaw.m*: yawed flow correction;
7. *model_Wind.m*: wind components calculation;
8. *model_DynamicStall.m*: dynamic stall routine;
9. *plot_Blades.m*: plot to monitor quantities of interest;
10. *plot_Rotating.m*: plot to monitor a sketch of rotaing wind turbine.

The output of the simuluation is saved as a *.mat* file, which cointains all the calculated results for each blade and at each time step. Finally, further scripts are required and used to achieve an accurate post processing.

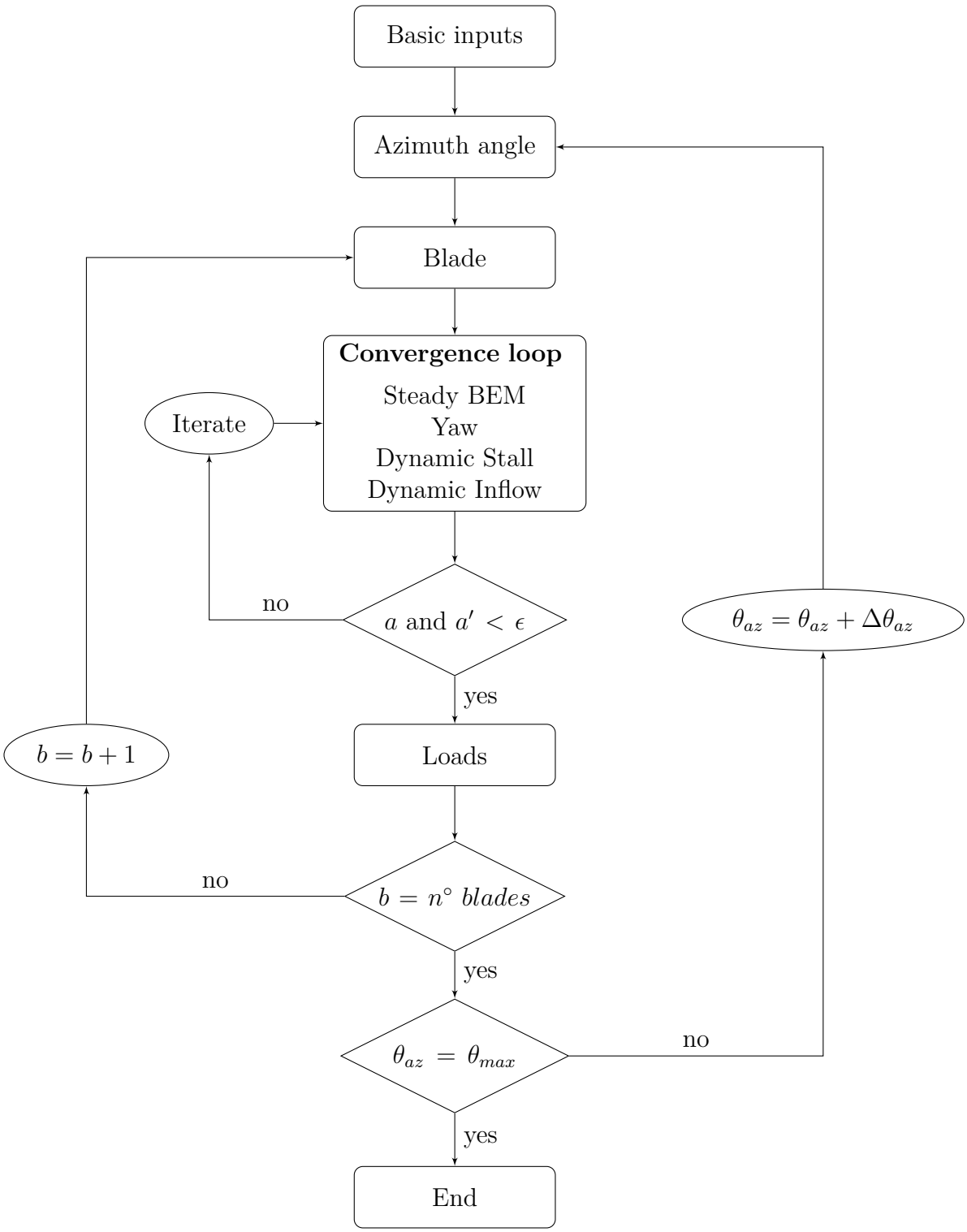

Figure 3.2: *Flow chart of Unsteady Blade Element Momentum (UBEM).*

- IV -

Yaw model

The purpose of the following chapter is to show the development and validation of a yaw model function to be coupled with the current BEM code in order to improve its prediction capabilities; changes required to the original algorithm are discussed.

4.1 Yawed flow modelling

The unsteady aerodynamic phenomena associated with yawed wind turbines are still poorly understood and are therefore challenging to be predicted accurately using a 1D model. The main issues concern the geometry of the skewed vortical wake formed behind the turbine, the unsteady flow field at the rotorplane induced by the vortical wake, as well as the aerodynamic effects of unsteady flow over the blade sections. Despite these difficulties, some of the widely adopted yaw corrections are implemented in the code; results are thus reported and commented, taking into account both the complexity of the phenomena and the simplicity of the adopted models. Advantages and drawbacks of the approach are exposed with some guidelines to write more realible models for wind turbine design codes.

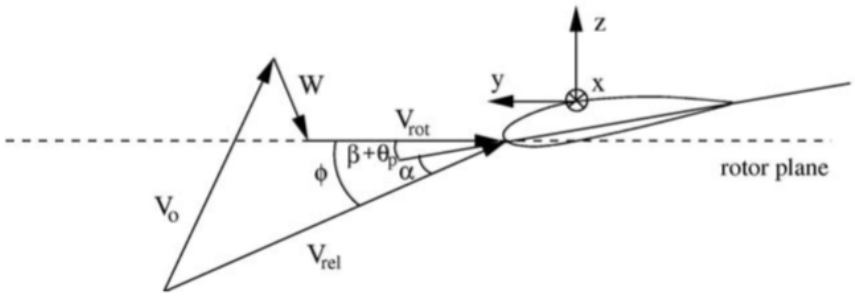

Figure 4.1: *Local flow in yawed wind.*

During normal operating conditions, wind turbines generally are subjected to a yaw angle relative to the incoming wind flow direction: wind velocity, V_0, is no longer orthogonal the rotor plane and it has both axial and tangential components, as shown in Figure 4.1. For a yawed rotor, a steady BEM code cannot reproduce the azimuthal variation of the involved parameters during the simulation, such as induced and relative velocities, flow angle, angle of attack and so on. The yawed condition implies a cyclic angle of attack and causes the helical wake behind the rotor to become skewed, yielding a time-dependent

induced velocity distribution on the rotor plane. For these reasons a yaw model has to be included into the unsteady structure of the code, as explained in Chapter 3.

The physical explanation of the behaviour of a yawed rotor deals with the fact that when the blade is pointing upstream the axial induction factor will be smaller than when the same blade, half a revolution later, is pointing downstream, because a blade pointing downstream is deeper into the wake. In the upwind half of the revolution a blade has mean induced velocities greater than those in the downwind rotation; this means that an upstream blade sees higher wind and bears higher loads than the downwind blade. Experiments have shown that ignoring the yaw correction leads to an unrealistic zero-restoring yawing moment. Therefore, the BEM method should be corrected for yawed flow condition to take into account the wake skew angle and the time dependency of the involved phenomena. Due to yawed rotor, the relative velocity changes its magnitude and direction during the blade's revolution, as depicted in Figure 4.2; a time dependent tangential component of wind velocity does exist, so the flow angle has to be calculated as follows:

$$\phi = \arctan \frac{V_{rel,z}}{-V_{rel,y}} = \arctan \frac{V_0(1-a)\cos\theta_{yaw}}{\omega r(1+a') - V_0 \sin\theta_{yaw}\cos\theta_{az}} \tag{4.1}$$

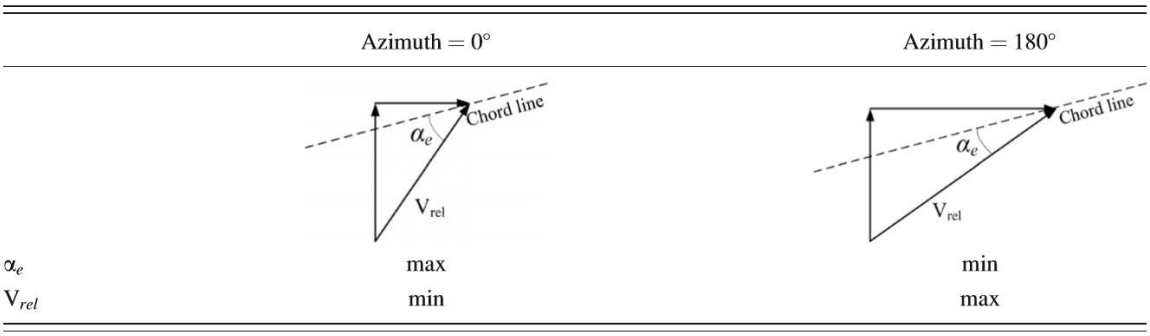

Figure 4.2: *Local flow in yawed wind.*

Several engineering models were added to BEM codes with the aim of improving their accuracy in predicting aerodynamic loads for yawed flows: they try to correct the axial induction factor, computed by BEM, for the uneven axial induced velocity distribution, that occurs at the rotorplane due to skewed wake. Glauert proposed in [12] a simple first harmonic non-uniform model which generates an induced velocity field that increases longitudinally from the leading edge to the trailing edge of the rotor disc as:

$$a_{yaw} = a\left(1 + K\frac{r}{R}\sin\theta_{az}\right) \tag{4.2}$$

Equation 4.2 was derived from the smoke visualization of the fully roll-up strong tip vortex, formed on helicopter rotors in forward flight. Much of the work of early experiments in yawed wind turbine were aimed at understanding the wake expansion and deflection. According to different authors, various models for K have been proposed to correct the asymmetric wake induction:

$$K = \tan\frac{\chi}{2}, \quad (Coleman\ et\ al.) \tag{4.3}$$

$$K = \sqrt{2}\sin\chi, \quad (While\ \&\ Blake) \tag{4.4}$$

$$K = \frac{15\pi}{32}\tan\frac{\chi}{2}, \quad (Pitts\ \&\ Peters) \tag{4.5}$$

$$K = \sin^2\chi, \quad (Howlett) \tag{4.6}$$

where the wake skew angle, χ, is defined as the angle between the wind velocity in the wake and the rotational axis of the rotor as depicted in Figure 4.3, and it is usually approximated as:

$$\chi = (0.6a + 1)\,\theta_{yaw} \tag{4.7}$$

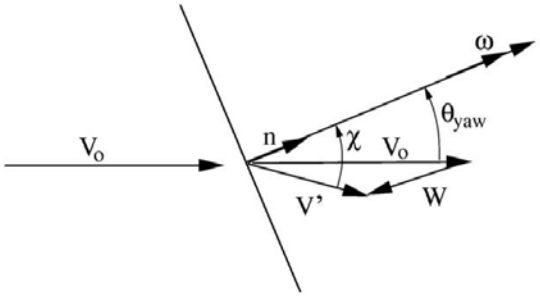

Figure 4.3: *Yawed rotor disc in wind field.*

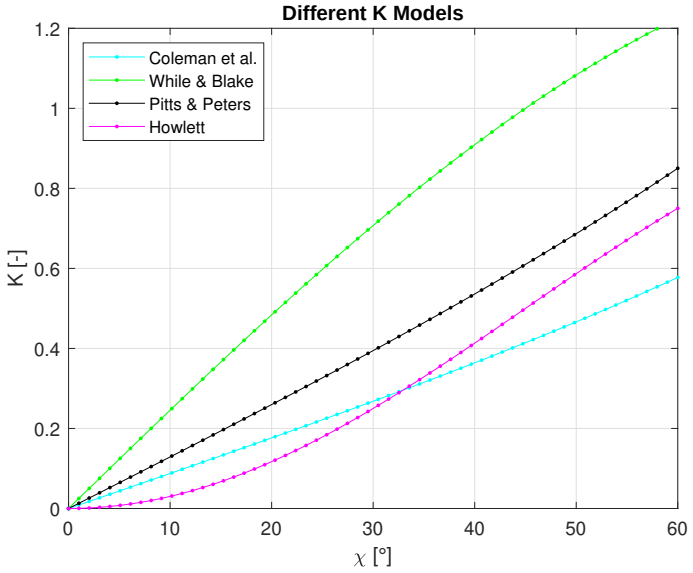

Figure 4.4: *Formulations of K for yawed flow.*

In Figure 4.4 the K models from Equation 4.3 to Equation 4.6 are represented, all different formulations are implemented and investigated in the unsteady BEM code. From a general point of view, all expressions contain a product between two functions: the first

one depends on the skew angle and second one is given as an expansion of the radial position: the more precise these functions, the more accurate is the prediction. Some discrepancies appear between the different values of K, so a best fitting technique with experimental data should be a selection criterion, because the value of the skew angle deeply affects the results of the calculation.

Regarding this, Øye proposed a new formulation, similar to the Glauert correction's, but with the introduction of a radial variation of the induction factor, based on a curve fitting procedure from an actuator disc vortex ring model. So, the corrected axial induction factor for yawed wind depends on the skew angle, azimuthal position of the blade and span:

$$a_{yaw} = a\left(1 + f_2 \tan\frac{\chi}{2}\sin\theta_{az}\right) \tag{4.8}$$

where the value of f_2 is found in [13] as a series expansion of radial position:

$$f_2 = \frac{r}{R} + 0.4\left(\frac{r}{R}\right)^3 + 0.4\left(\frac{r}{R}\right)^5 \tag{4.9}$$

In [14] Blondel et al. proposed another formulation for the induction factor of the New Mexico wind turbine in yawed conditions, derived from coupling experimental data with vortex model and CFD simulations:

$$a_{yaw} = a\left[1 + k_1\frac{r}{R}\tan\frac{\chi}{2}\sin\left(\theta_{az} + \phi_1\right) + k_2\left(1 - \frac{r}{R}\right)\tan\frac{\chi}{2}\sin\left(\theta_{az} + \phi_2\right)\right] \tag{4.10}$$

where, after some calibrations, phase angle and linear functions have been defined as:

$$\phi_1 = -\frac{\pi}{9}, \qquad \phi_1 = \pi, \qquad A_0 = 0.35 \tag{4.11}$$

$$k_1\left(\frac{r}{R}\right) = 1 - A_0 + A_0\frac{r - R_{hub}}{R_{tip} - R_{hub}}, \qquad k_2\left(\frac{r}{R}\right) = 1 - A_0\frac{r - R_{hub}}{R_{tip} - R_{hub}} \tag{4.12}$$

Although the resulting skewed wake geometry is more complex than the approximation of Equation 4.7, some positive results of these simple models have been achieved. However, some discrepancies still affect the yaw formulation, in particular the axial induction factor distribution of Equation 4.2 and Equation 4.8 would require some refinements to reduce gaps between predicted and experimental results.

4.2 Simulation results

The BEM code with yawed flow correction has been validated using the experimental dataset of NREL Phase VI horizontal axis wind turbine [10]. Different approaches in yaw correction have been investigated and compared. According to the results obtained, Øye's axial induction factor is the best solution, but some comparisons with other formulations are discussed.

4.2.1 Torque validation

To understand the physical phenomena involved, the behaviour of each blade is going to be described by the following remarks, referring to Øye's formulation. Figure 4.5 represents each blade's torque contribution: a periodicity as a sine curve can be seen due to an azimuthal variation of all parameters involved during the simulation. Remember that the azimuth angle is definded at zero position for blade number one at 12 o'clock; for blade number two its azimuth angle is shifted of 180°, as NREL Phase VI has a two bladed rotor. Blade number one starts to rotate counterclockwise if seen from upwind at 12 o'clock, from 0° to 90° its torque goes down because of the downwind condition and it reaches a minimum that means that the blade is deepest into the wake. Minimum position is not exactly at 90°, as expected: this is probably due to some phase lag not considered in this simple yaw model. Torque of the same blade starts increasing at 9 o'clock, but its value is still under the mean value, because the blade is still downwind. At 180° upwind conditions begin to appear, torque still goes up and at nearly 270° a maximum is reached. Finally, between 270° and 360° torque decreases, but its value is still above the mean value. Similar conditions occur for blade number two, but with a phase shift of 180°. To complete an accurate validation of the model, the following subsection will also investigate the normal force along the span according to different axial induction factor corrections.

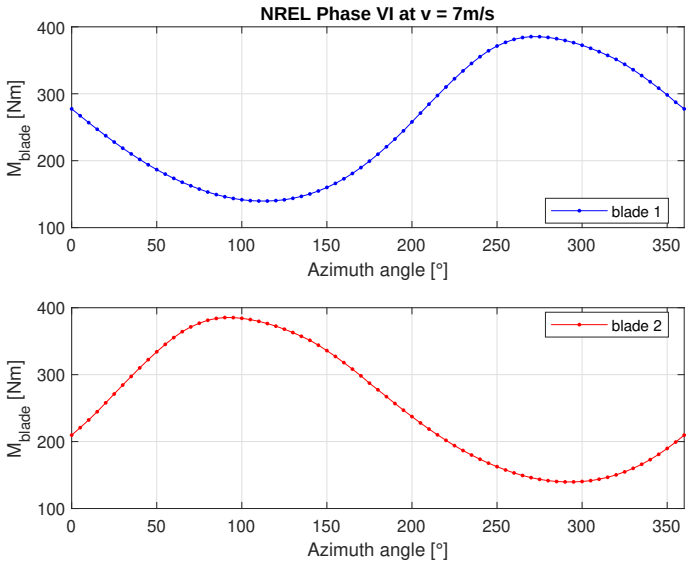

Figure 4.5: *Torque contribution of each blade.*

In order to validate the code and analyze the different solutions, experimental data of the low speed shaft torque at 30° yaw has been considered. Figure 4.6 and Figure 4.7 represent the torque trend at $5m/s$ and $7m/s$ during a complete revolution of the rotor, according to all yaw models analyzed in this work. These yaw formulation approaches give quite different results, as expected. At $5m/s$ Øye's model manages to catch the amplitude of the oscillating torque and the azimuth angle of its maximum and minimum values; While's formulation seems to overpredict the amplitude, instead the other ones underestimate the value of low speed shaft torque. At $7m/s$ Øye's and While's expressions

catch both the global trend of torque and azimuth angles of maximum and minimum power, as well as CFD simulation in [15]. The maximum value is well predicted by the code, with a reasonably accuracy, but its value is underestimated by approximately 3%. Howlett, Pitts and Coleman significantly underestimate the maximum power.

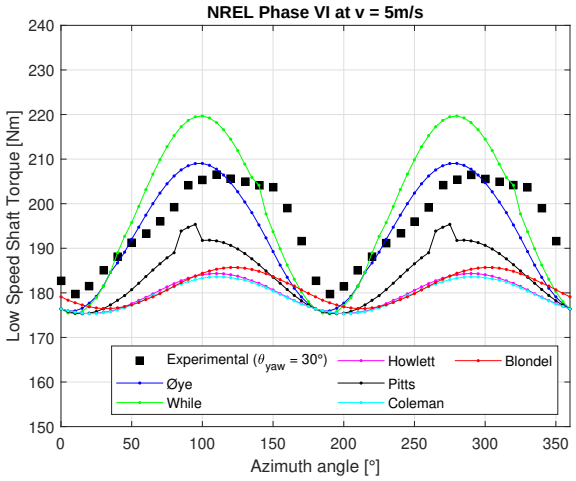

Figure 4.6: *Low speed shaft torque at* $5m/s$.

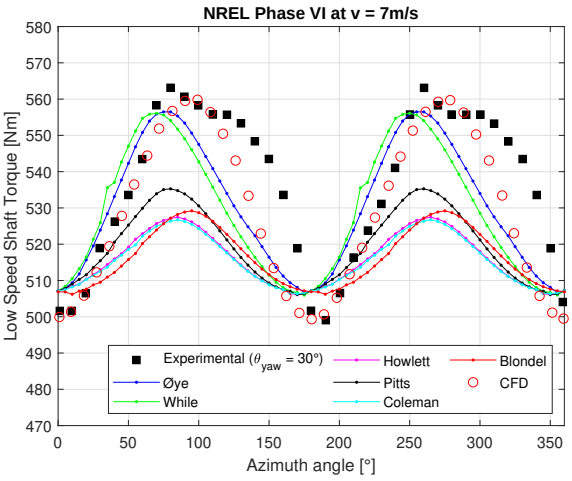

Figure 4.7: *Low speed shaft torque at* $7m/s$.

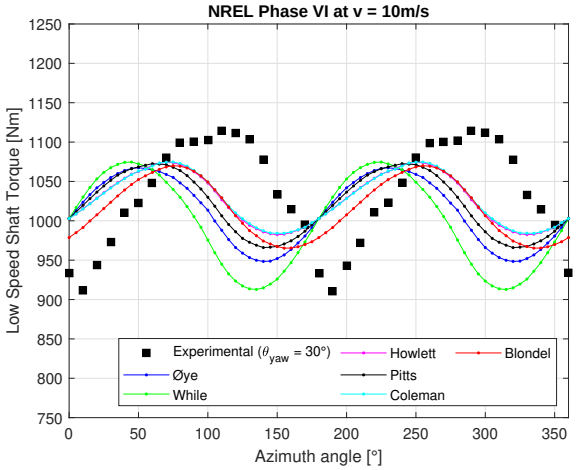

Figure 4.8: *Low speed shaft torque at* $10m/s$.

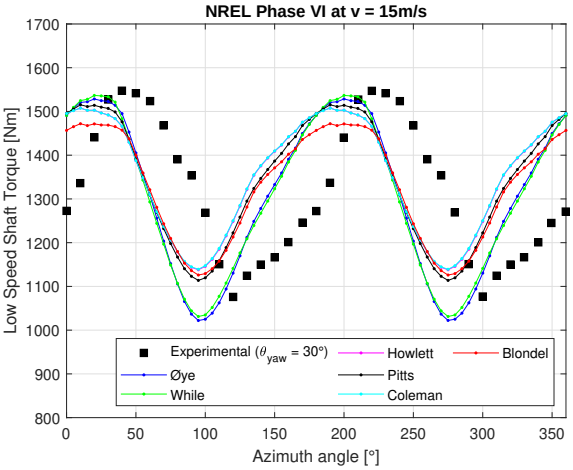

Figure 4.9: *Low speed shaft torque at* $15m/s$.

Figure 4.8 and Figure 4.9 represent the torque changes at $10m/s$ and $15m/s$. Some discrepancies are seen in both plots: at $10m/s$ a phase shift error of about 35° is evident, in particular Blondel and Coleman formulations are able to reduce this shift, even if the amplitude of the torque is better predicted by While's model. As revealed by a CFD analysis carried out in [11], the blade is subjected to stalled operating conditions at $10m/s$, so the inaccurate prediction may be caused by the spread of this strongly 3D phenomenon. At $15m/s$, a phase shif of about 45° appears, but the amplitude of low speed shaft torque is well predicted by each model.

Furthermore, it was necessary to apply a correction factor to the torque output given by the code, as represented in Figure 4.10, in order to fit the medium values of the experimental low speed shaft torque. The previous phase error and this scale correction

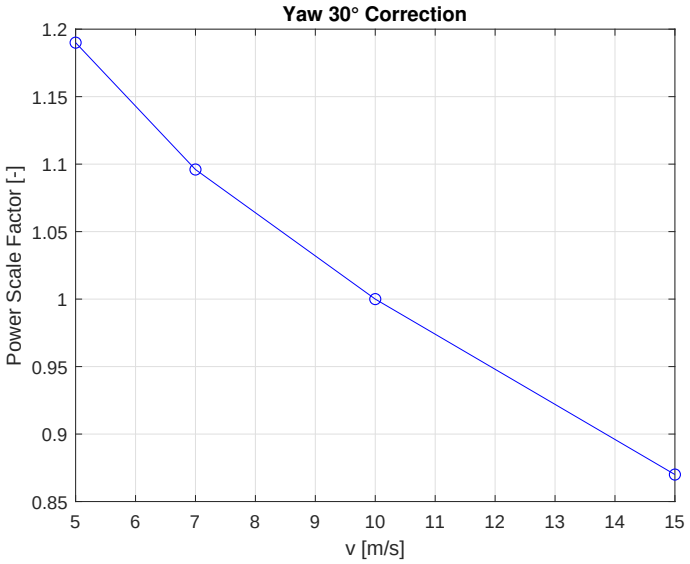

Figure 4.10: *Correction for* $\theta_{yaw} = 30°$.

reveal that these yaw models show some discrepancies, especially at high wind speed. This is because the BEM theory is not able to model the more complex and skewed wake created by a yawed turbine, consequently additional engineering models are required to correct the skewed wake effects in yawed operating conditions. In [16] a different approach of coupling the blade pressure measurements with the free wake vortex model has been established and integrated with the classical BEM model. This approach allows to estimate the unsteady induced velocity fields at the rotorplane of NREL Phase VI. In the same work, it is remarked that the free wake calculations confirm the periodic variation of axial induction factor with azimuth angle, but the results from skewed wake effects in yaw are far more different than the sinusoidal variation predicted by Glauert. This is mainly due to root vorticity effects which tend to be predominant in wind turbines, as opposed to what is usually seen in helicopter rotors in forward flight. More complex Fourier series should be taken into account to model the axial induction factor, for example in [16] is proposed:

$$\frac{a_{yaw}}{a} = 1 + \frac{A_0}{2} + A_1 \cos(\theta_{az} + \phi_1) + A_2 \cos(\theta_{az} + \phi_2) + A_3 \cos(\theta_{az} + \phi_3) \qquad 4.13$$

where the amplitudes A_0, A_1, A_2 and A_3 and the phases ϕ_1, ϕ_2 and ϕ_3 are modelled as a function of: yaw angle, radial position, tip speed radio and rotor geometry. Finally in [16] the predicition of the axial induction factor field by the free wake model makes possible to calculate the required values in Equation 4.13 to obtain an accurate prediction of the aerodynamics in yawed condition. A big limit of the model is that the just calculated amplitudes and phases are consistent for fixed rotor geometry and operating conditions.

4.2.2 Normal force validation

Furthermore, experimental data of normal force per unit area distribution is also available in [17]; the normal force to the rotor plane can be calculated for a single layer from the following equation:

$$F_N = \frac{1}{2}\rho V_{rel}^2 \left(C_L \cos\phi + C_D \sin\phi\right) \tag{4.14}$$

The calculated normal forces using BEM with Øye and Coleman corrections are represented from Figure 4.11 to Figure 4.18 at spans of 47%, 63%, 80%, 95% and wind speeds $10m/s$ and $15m/s$. No scale factors have been applied. The blade starts to rotate counterclockwise if seen from upwind at zero azimuth at 12 o'clock and goes across the half downwind side of the rotor plane, normal force goes up until it reaches a maximum value at 180° azimuth position, *i.e.* at 6 o'clock. The normal force is well predicted by both formulations, in terms of phase and amplitude of the oscillating trend, except for some unexpected variations in Figure 4.12 and Figure 4.14, probably due to a big variation of extrapolated lift and drag coefficients in a small range of angles of attack. Between Øye and Coleman formulations, no evident differences are noticed in normal force prediction at inboard and medium sections; but some discrepancies are observed at spans 80% and 95%, as it can be seen in Figure 4.15, Figure 4.17 and Figure 4.18. As said in [17], at the tip region is not easy to accurately predict experimental data, since tip loss factor does not manage to catch all phenomena occurring in that region, due to high relative speed, turbolence and tip vortex.

Despite these problems, Pitts, Coleman and Blondel methods are more accurate than Øye's approach, as Figure 4.19, Figure 4.20 and Figure 4.21 show, even if the last formulation is calibrated for the New Mexico wind turbine. Coleman formulation achieves a good matching in normal force prediction, but, on the other hand, it underestimates the oscillating amplitude of torque in Figure 4.9 and Figure 4.8, compared to Øye's and While's formulations.

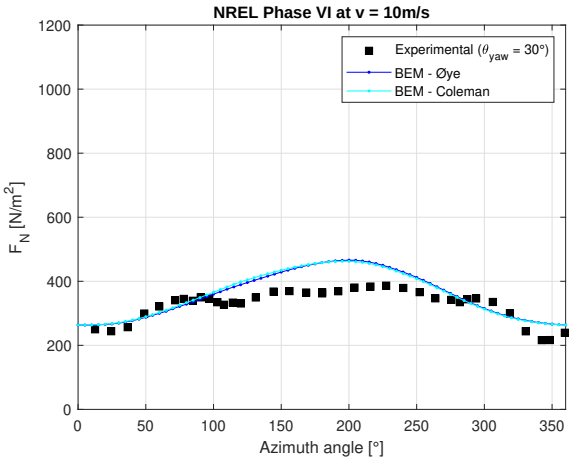

Figure 4.11: *span 47%.*

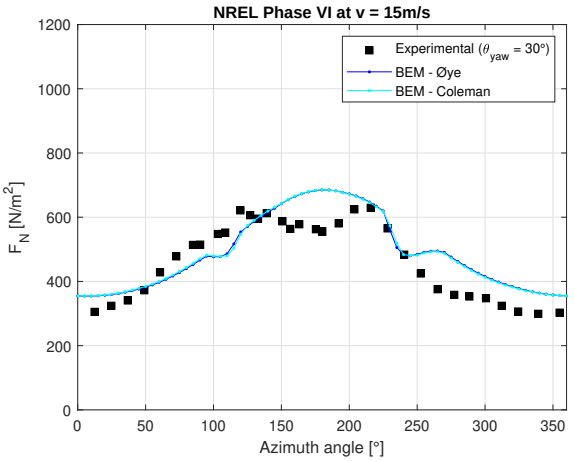

Figure 4.12: *span 47%.*

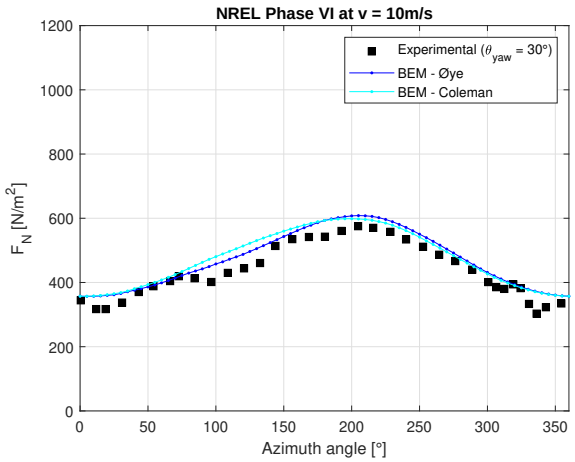

Figure 4.13: *span 63%.*

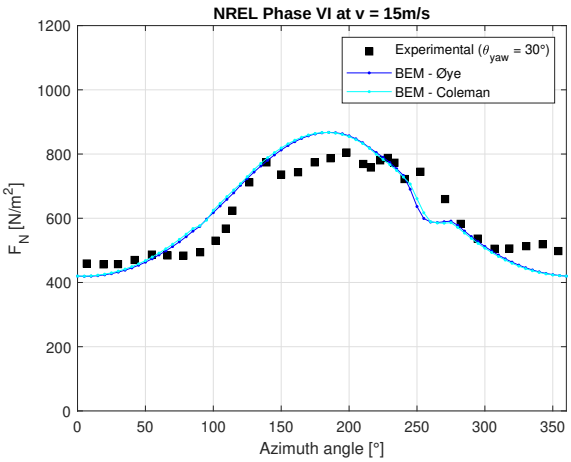

Figure 4.14: *span 63%.*

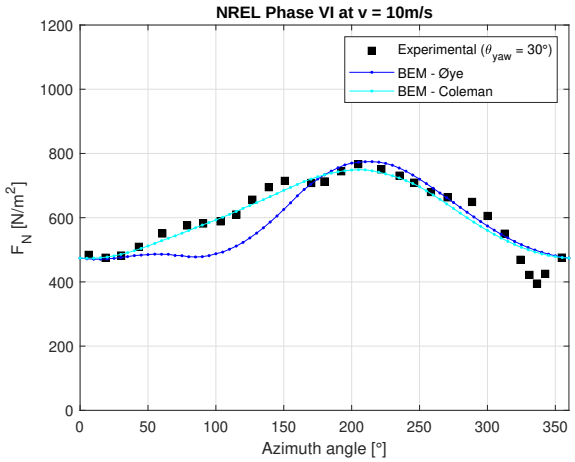

Figure 4.15: *span 80%.*

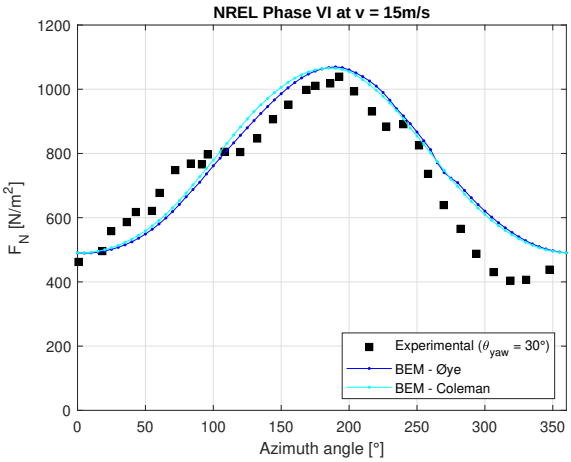

Figure 4.16: *span 80%.*

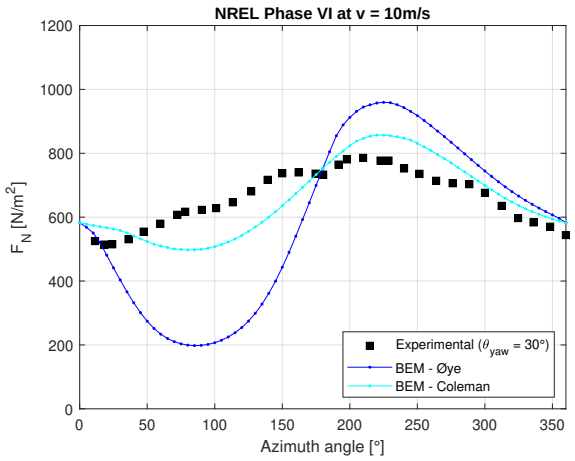

Figure 4.17: *span 95%.*

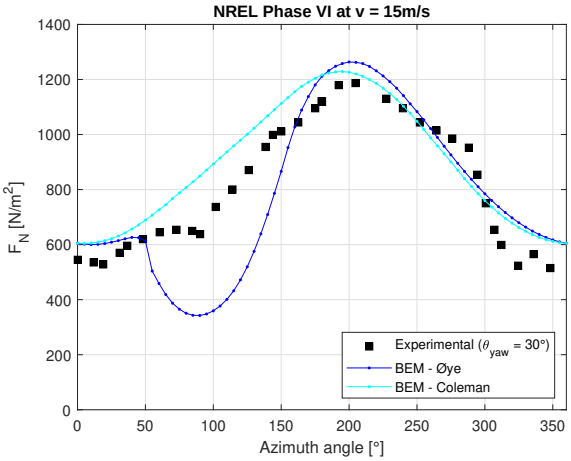

Figure 4.18: *span 95%.*

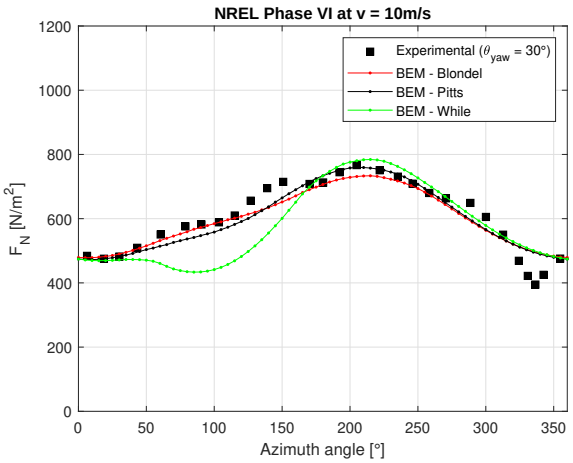

Figure 4.19: *span 80%.*

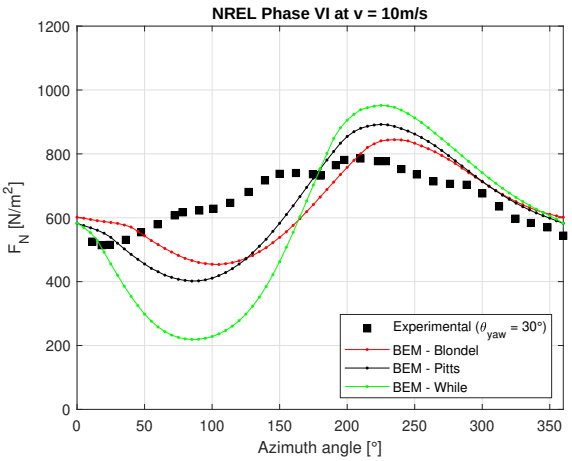

Figure 4.20: *span 95%.*

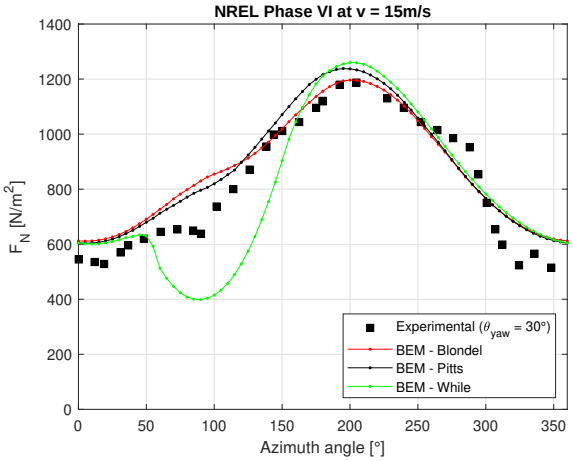

Figure 4.21: *span 95%.*

Furthermore, some considerations have to be taken into account concerning the angle of attack and axial induction factor plots. The effective angle of attack on the blade varies with the azimuth angle under the influence of yawed inflow, in [18] it is shown that phase shifts of angle of attack distribution does exist between different radii. The same behaviour has been found in this work as represented in Figure 4.22: the lowest angle of attack occurs at 180° azimuth position at the blade near-root section, while it shifts to below 180° at the near-tip section. This is reasonable because the wake produces a greater influence on the blade near-tip region.

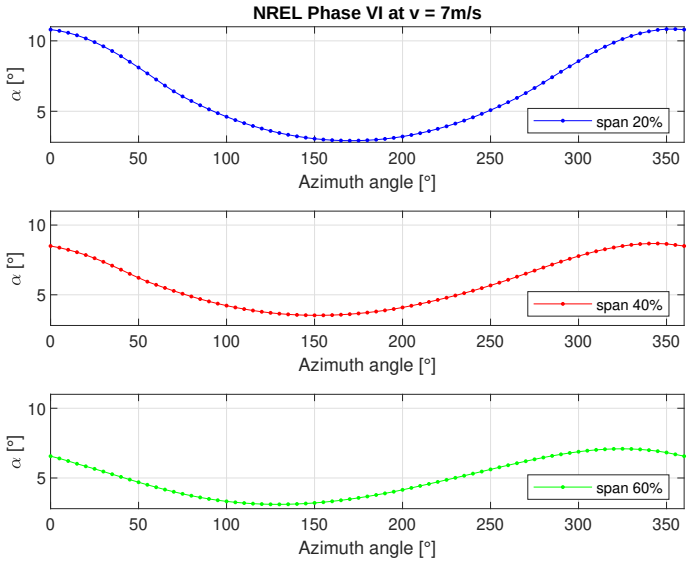

Figure 4.22: *Angle of attack under 30° yawed wind.*

Finally, Figure 4.23 represents axial induction factor in case of wind speed $7m/s$ and 30° yaw angle. Between 0° and 180°, downwind condition for the first blade occurs, the blade is deeper into the wake and induced velocity grows. During the other half revolution, the same blade deals with the upwind condition, so smaller axial induction factors, higher angle of attack and higher mean blade's torque occur than during the downwind state. Axial induction factors reveal maximum and minimum values approximately at the same azimuth angle; the already discussed changes in minimum value of angle of attack are linked to different velocity triangles and, in particular, if axial induction does not present a remarkable phase shift, a more evident one is seen in Figure 4.24, which represents tangential induction factor variation during a complete blade revolution.

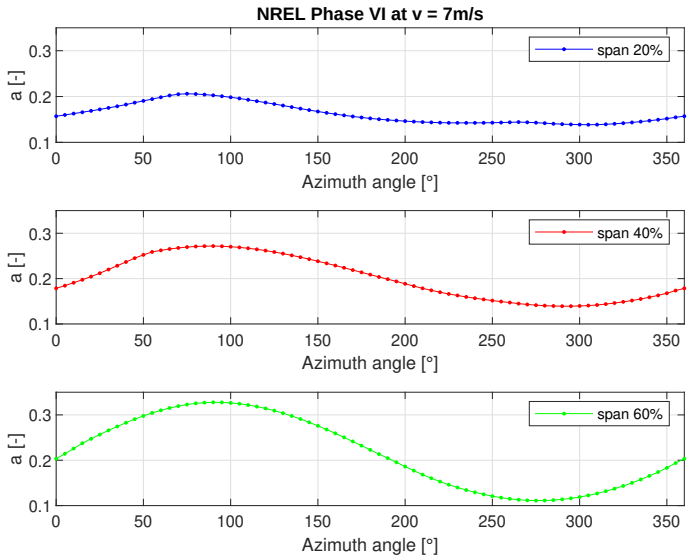

Figure 4.23: *Axial induction factor.*

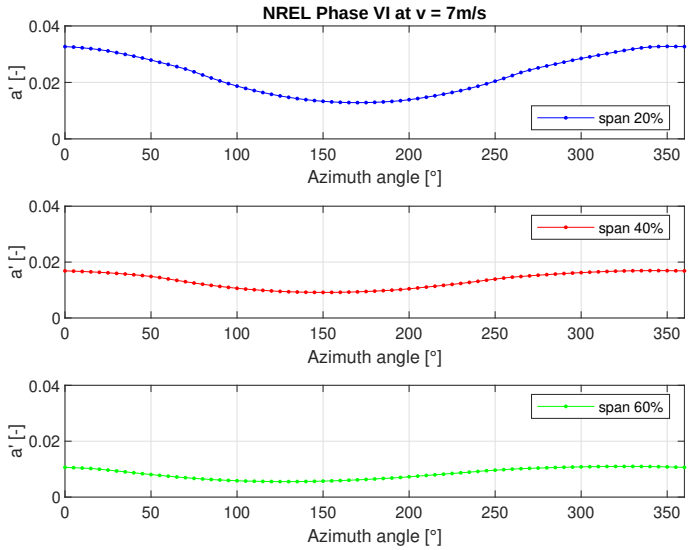

Figure 4.24: *Tangential induction factor.*

- V -

Dynamic stall model

The purpose of the following chapter is to show the development and validation of a dynamic stall model to be coupled with the unsteady BEM code; changes carried out in the algorithm are thus discussed. Results applying different models in the unsteady BEM code are explained.

5.1 Unsteady airfoil aerodyinamics

The unsteadiness of airfoil behaviour has not been considered yet, so a dynamic stall model for lift coefficient is here presented. Until 50'*s* this phenomenon was only studied experimentally, the first analytical dynamic stall models were introduced in the late 70'*s*, [19]. As explained in Chapter 4, the local angle of attack changes dynamically during a complete revolution of the rotor due to yaw or tilt misalignment. The effect of changing the blade's angle of attack does not appear instantaneously on loads, but will take place with a time delay proportional to the chord divided by the relative velocity seen by the blade's layer.

Since the complexity and the quite recent approach of dynamic stall applied to wind turbines, a lot of different models are available in literature. This work refers to two main models: the original Beddoes-Leishman model, with some modifications explained in [19], for the trailing edge separation, and the model described by Øye in [3] and [19] for the dynamic model of trailing edge separation.

5.1.1 Trailing edge separation model

The original Beddoes-Leishman model includes attached flow, leading edge separation and impulsive forces due to compressibility. For wind turbines, Mach number is lower than the limit value of 0.3, so the flow is assumed incompressible; furthermore the vortex caused by the leading edge separation may be neglected as a non-dominating phenomenon for wind turbine blades, whose airfoil have thicknesses equal or greater than 15%. These assumptions lead to an alternative formulation of the original Beddoes-Leishman model where the lift under attached flow conditions is given by the Theodorsen theory and only trailing edge separation is considered under stalled flow conditions.

The basic assumption of Beddoes-Leishman trailing edge separation approach is that the static lift curve can be represented by a nonlinear function of the angle of attack as:

$$C_l^{st}(\alpha) = C_{l,\alpha}\left(\frac{1+\sqrt{f_s^{st}(\alpha)}}{2}\right)^2(\alpha-\alpha_0) \tag{5.1}$$

which is the lift coefficient on a flat plate in a potential Kirchhoff flow. The constant $C_{l,\alpha}$ is the slope of the lift curve in the linear region of attached flow and the static separation function $f_s^{st}(\alpha)$ determines the separation point referring to the trailing edge separation. The flow is fully attached for $f_s^{st} = 1$ and fully separated for $f_s^{st} = 0$, as sketched in Figure 5.1.

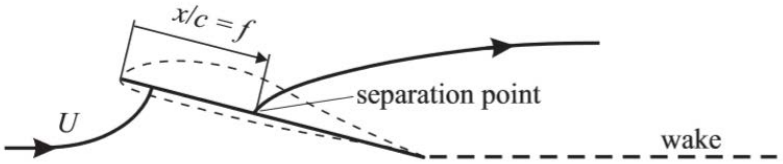

Figure 5.1: *Trailing edge separation point.*

The static lift curve is given by the polar table, so $C_l^{st}(\alpha)$ is known; the next step is to calculate α_0 as an interpolation of given lift curve at zero angle of attack. Furthermore, the slope $C_{l,\alpha}$ of the lift in the linear curve is evaluated as:

$$C_{l,\alpha} = \max_{i=1,\ldots,\bar{\alpha}}\left(\frac{C_l^{st}(\alpha)}{\alpha-\alpha_0}\right)_i \tag{5.2}$$

and from Equation 5.1 the separation point can be calculated as a function of the angle of attack:

$$f_s^{st}(\alpha) = \left(2\sqrt{\frac{C_l^{st}(\alpha)}{C_{l,\alpha}(\alpha-\alpha_0)}} - 1\right)^2 \tag{5.3}$$

Two conditions have to be taken in consideration: the first is that the separation point cannot exceed the trailing edge of the airfoil; second one is that Equation 5.1 is not valid beyond the angles of attack α^{+fs} and α^{-fs}, where the separation point function is set to zero, $f_s^{st} = 0$.

In case of angles of attack exceeding the limit of fully separation, the static lift curve is represented as the sum of fully attached and fully separated flow contributions by a linear interpolation:

$$C_l^{st}(\alpha) = f_s^{st}(\alpha)\,C_{l,\alpha}(\alpha-\alpha_0) + C_l^{fs}(\alpha)\left(1-f_s^{st}(\alpha)\right) \tag{5.4}$$

where the lift coefficient for fully separated flow is computed as:

$$C_l^{fs}(\alpha) = \frac{C_l^{st}(\alpha) - C_{l,\alpha}(\alpha-\alpha_0)\,f_s^{st}(\alpha)}{1-f_s^{st}(\alpha)} \tag{5.5}$$

By using Equation 5.5 the fully separated lift coefficient cannot be calculated in the fully attached region, *i.e.* when $f_s^{st} = 1$; however, by substitution of Equation 5.3 in Equation 5.5 it can be shown that:

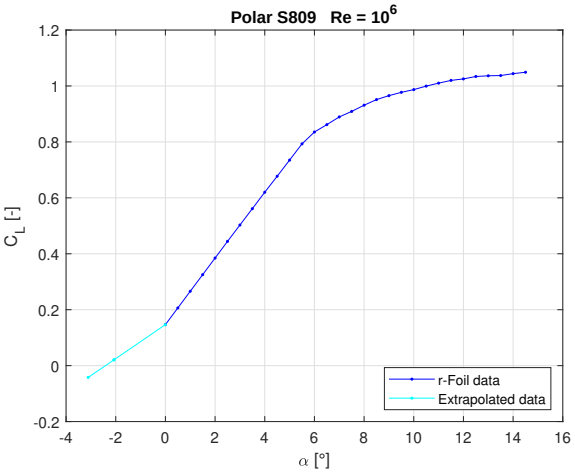

Figure 5.2: *Different slope between original and extrapolated data in the linear region.*

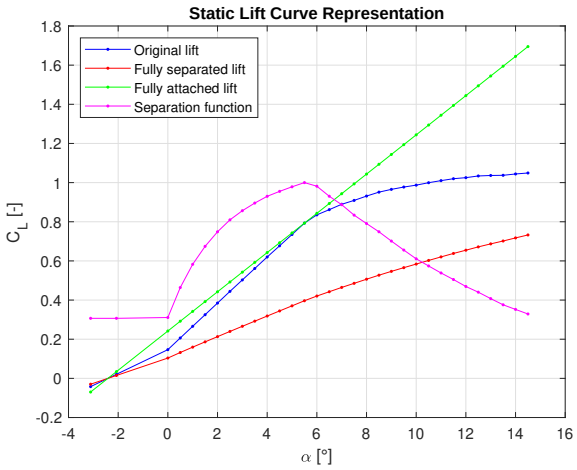

Figure 5.3: *Contributions to the lift curve of S809 airfoil at* $Re = 10^6$.

$$C_l^{fs}(\alpha) \to \frac{C_l^{st}(\alpha)}{2} \quad \text{when } f_s^{st} \to 1 \quad \text{for } C_{l,\alpha}(\alpha - \alpha_0) \to C_l^{st}(\alpha) \tag{5.6}$$

hence, the lift for fully separated flow at low angles of attack is half the lift for fully attached flow.

Polar tables have been calculated for angles of attack starting from 0° to the maximum value reached by panel codes, so the values of angles beyond this interval are results of the extrapolation already mentioned in Chapter 2. Figure 5.2 shows that the linear region for negative angles of attack presents a lower slope than the region of positive angles of attack and this has a direct influence on the maximum slope, evaluated by Equation 5.2. In Figure 5.3 are represented the contributions of fully attached and fully separated lift to the static polar of S809 airfoil at Reynolds number 10^6. As the angle of attack at zero lift α_0 belongs to the extrapolated curve of lower slope in Figure 5.2 and as the value of Equation 5.2 depends on α_0, it is quite simple to justify why the lift coefficient is slightly different to the fully attached one in the linear region in Figure 5.3. In particular, if the slope of extrapolated and *rFoil* curves in Figure 5.2 was the same one, the separation point function would be closer to unity.

5.1.2 Dynamic model of trailing edge separation

Even if previous considerations seem not related to unsteady airfoil phenomena, they are required for a proper formulation of a dynamic stall model. According to Øye's formulation the value of the separation point function changes dynamically during the blade's revolution, in other worlds it depends on time. For trailing edge dynamic stall the degree of stall is based on the following equation:

$$C_l^{dyn}(\alpha, t) = f_s(t)\, C_{l,\alpha}(\alpha - \alpha_0) + C_l^{fs}(\alpha)\left(1 - f_s(t)\right) \tag{5.7}$$

that is similar to Equation 5.4, but with the introduction of the time dependency in the separation point function. The assumptions is that the separation point function tries to

get back to the static value, thanks to a first order differential equation that represents the time delay in the motion of the separation point:

$$\frac{df_s}{dt} = \frac{f_s^{st} - f_s}{\tau} \tag{5.8}$$

where f_s^{st} is the value of f_s which reproduces the static airfoil data if applied in Equation 5.4 and the time constant τ is:

$$\tau = \frac{4c}{V_{rel}} \tag{5.9}$$

Equation 5.8 can be integrated analytically to give the separation point at the following time step as a function of its value assumed in the current time step:

$$f_s\left(t + \Delta t\right) = f_s^{st} + \left(f_s\left(t\right) - f_s^{st}\right) e^{-\frac{\Delta t}{\tau}} \tag{5.10}$$

At time $t_1 = 0s$, the static lift coefficient is used; at the second time step the value of $f_s(t_2)$ can be evaluated from $f_s(t_1)$ and thus the dynamic lift is now included in the BEM iterations. The exposed set of equations needs to be developed in a routine coupled with the BEM algorithm, as previously done for the yaw model. The main steps are here summarized:

1. Find the angles at zero lift with an interpolation of polar tables;
2. Find the maximum linear lift slope using Equation 5.2;
3. Calculate the separation point function using Equation 5.3 and the original lift curve;
4. Calculate the fully separated lift coefficient using Equation 5.5;
5. Calculate time constant with Equation 5.9;
6. Solve differential equation thanks to Equation 5.10;
7. Calcutate dynamic lift coefficient using Equation 5.7.

Attention has to be given to steps 1 and 2, as both the angles of zero lift and the maximum linear lift slope are functions of Reynolds number too. So those steps have to be handled as explained in Chapter 2, applying the Reynolds interpolation routine.

Øye's model has the advantage of being simple because the input is only the static polar of the airfoil; on the other side, the dynamic effects are represented only by one state variable, $f_s(t)$, that includes time delay for separated flow, but no dynamic effects are introduced during attached flow conditions. To underline the importance of the dynamic stall formulation for wind turbines, Øye demonstrated that non-existent flapwise vibrations may result from the calculation, especially for a stall-regulated machine, if a dynamic stall model is not used. A variety approaches of different complexities for modelling dynamic stall is available in [20], such as the Beddoes-Leishman model, ONERA model, Risø model and Boeing-Vertol model; finally in [19] it is shown how the unsteady lift influences the unsteady drag and moment coefficients too.

5.2 Validation

The validation of dynamic stall model has been conducted for NREL Phase VI horizontal axis wind turbine, whose blade's airfoil is the S809 profile. The turbine is in yawed operating condition, so the local angle of attack changes with a sinusoidal shape during the blade's revolution, as explained in Chapter 4 and depicted in Figure 4.22. First of all a complete review of the experimental conditions is given, then the results of the simulation are commented. The first part of the validation focuses on the dynamic lift as a result of the wind turbine simulation; the second one refers to a comparison with the previous yaw model results.

5.2.1 Experimental setting

Normally, experimental data of dynamic lift coefficients refers to 2D measurements carried out for a single airfoil instead of an entire blade. The S809 airfoil was tested under steady and unsteady conditions by The Ohio State University Aeronautical and Astronautical Research Laboratory (OSU/AARL) in a subsonic wind tunnel sketched in Figure 5.5 and Figure 5.6. A detailed experimental setting's report is described in [20], whose results are given in terms of lift, drag and moment coefficients as a function of the angle of attack which changes dynamically in time. Furthermore, in [21], [22] and [23], the results for S812, S813 and S814, respectively, are reported after similar experimental tests. A cam mechanism connected to the airfoil makes a sinusoidal pitch oscillating motion of the airfoil through an orthogonal axis at 25% of the chord:

$$\alpha(t) = \alpha_m + A\sin(2\pi f t) \tag{5.11}$$

Experimental conditions are characterized by: mean angle, amplitude and frequency of the oscillation, but also by Reynolds number of the flow and by a dimensionless geometrical parameter, known as reduced frequency, that represents the unsteadiness of the flow:

$$\omega_{red} = \frac{\Omega c}{2U} \simeq \frac{\omega c}{2\omega r} = \frac{c}{2r} \tag{5.12}$$

where U is the mean velocity and Ω is the characteristic frequency of the unsteady flow, whose periodic change seen by the blade layers occurs at the same frequency of the rotation of the rotor. The set of experimental conditions employeed by OSU is summarized in Table 5.1.

mean oscillation angle [°]	α_m	8; 14; 20
oscillation amplitude [°]	A	± 5.5; ±10
pitching frequency $[Hz]$	f	0.6; 1.2; 1.8
Reynolds number $^*10^{-6}$ [−]	Re	0.75; 1.0; 1.25; 1.4

Table 5.1: *OSU experimental settings.*

As suggested in [24], the effective velocity is assumed to be mainly dominated by tangential velocity component, ωr, that leads to the final expression of Equation 5.12. According to [24], the flow is considered as quasi-steady for $0 < \omega_{red} \leq 0.05$, if $0.05 < \omega_{red} \leq 0.2$ is treated as unsteady, otherwise it is highly unsteady. However, in [25] unsteady flow regime for wind turbine is said to occur for $\omega_{red} > 0.02$. The spanwise distribution of the reduced frequency for NREL Phase VI wind turbine is represented in Figure 5.4. It can be seen that until span 12% layers experience an highly unsteady flow; from 12% to 81% spans, the flow is unsteady, otherwise it is quasi steady.

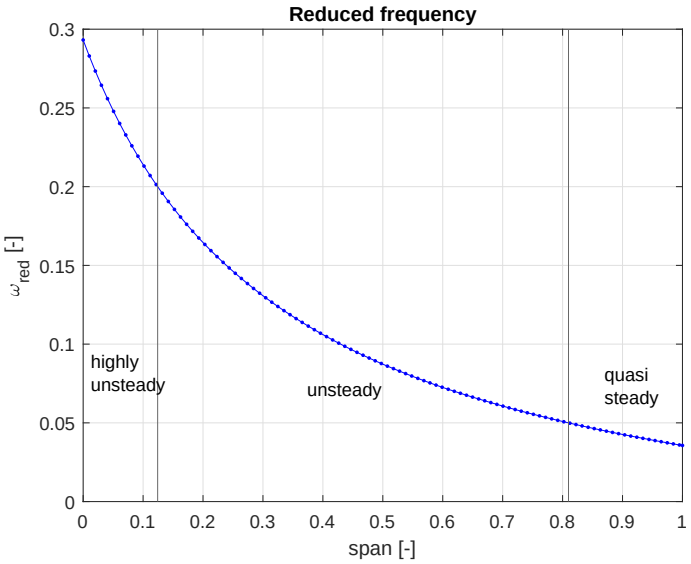

Figure 5.4: *Spanwise reduced frequency for NREL Phase VI.*

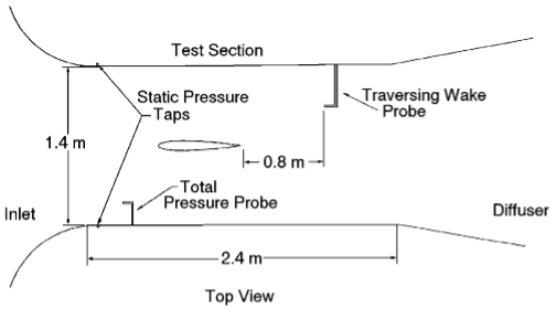

Figure 5.5: *Top view of subsonic wind tunnel.*

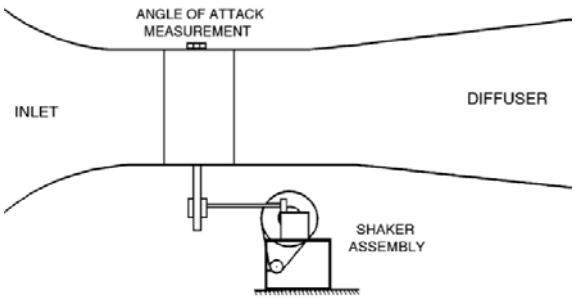

Figure 5.6: *Side view of subsonic wind tunnel.*

5.2.2 Dynamic lift results

During the unsteady simulation the local angle of attack changes in a sinusoidal way because the turbine operates under 30° yawed conditions; on the other hand, the pitch motion forces the variation of the angle of attack in the experimental tests. Considering this background, a comparison may be established between experimental data and simulation results, if the same geometrical and flow motion conditions are reproduced both by

experimental tests and unsteady BEM simulation. In particular: mean angle, amplitude and frequency of the oscillating motion, but also Reynolds number and reduced frequency must be sufficiently similar.

To make a proper and correct comparison, a span where the same conditions are well reproduced has been selected. In particular, as the Reynolds number at a fixed span is not constant in the unsteady BEM simulation, the mean value during a complete blade revolution has been considered. The frequency of the pitch motion of experimental data, f, has been chosen according to the angular velocity of NREL Phase VI rotor, as $f = \omega/(2\pi)$. It is important to underline that the OSU test was carried out for an isolated airfoil, whereas in the present work an entire blade has been simulated by a BEM algorithm. However, the BEM code does not take in account spanwise flow motion, so each 2D layer is treated as an isolated profile.

The following plots show the results in terms of dynamic lift coefficient and angle of attack at a fixed span; the table below each plot summarizes OSU testing and experimental conditions. Figures on the right hand side of the following pages represent the trend of angle of attack and lift coefficient as functions of the azimuth angle or, equally, of time, as $\theta_{az} = \omega t$. As expected, the introduction in the code of dynamic stall influences only the lift coefficient, without evident effects in the angle of attack which does not change its trend derived with yaw model only. Plots on the left hand side of the pages shows a comparisson between the hysteresis loop of experimental data and lift coefficient as result of the simulation. The dispersion of experimental data is evident, as remark of the unsteadiness of dynamic stall.

Although Øye's model is one of the most simple and dynamic stall phenomenon itself involves a non-linear flow behaviour, the proposed solution reproduces the position of the hysteresis loop in the plane and also its amplitude; in particular for mean oscillation angle of 8°, as Figure 5.7 shows, a precise amplitude results is not provided by the model, for example the maximum error on amplitude loop is about 15%. However, the other plots give a more accurate prediction of both trend and amplitude. The discrepancy with experimental data points is related to the turbolence phenomena occuring in wind turbine applications, so a better fit would require higher fidelity models, with increased calculation and implementation time. These plots have to be read at first considering the oscillation intervals in the table below; then the geometrical parameter, reduced frequency and finally attention should be focused on Reynolds number that mildly influences the polar.

Figure 5.7 to Figure 5.12 refer to the NREL Phase VI horizontal axis wind turbine; clearly the dynamic stall loop appears more evident at high wind speed, due to stall. Wind velocity and thus the degree of the blade's layer stall deeply affects lift versus azimuth plots, where the differences between the new curve and the previous one are related with the activation of the dynamic stall model in the code.

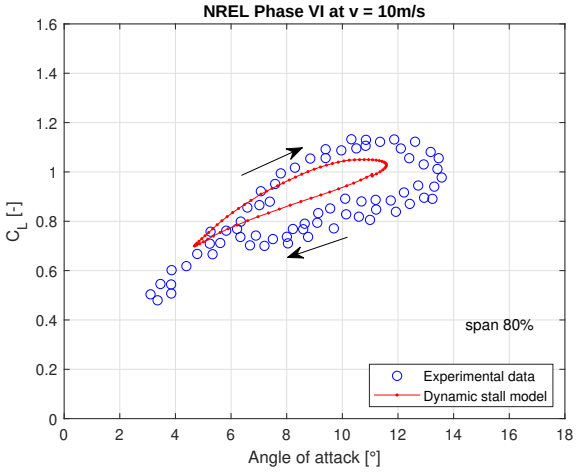

Figure 5.7: *Dynamic stall hysteresis loop.*

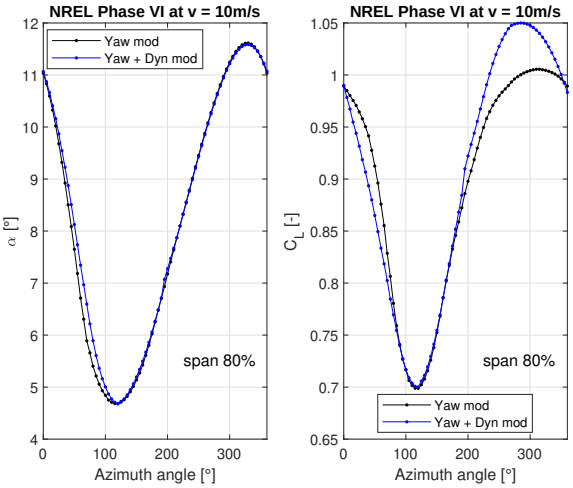

Figure 5.8: *Angle of attack and lift coefficient.*

	OSU testing conditions	Simulation conditions
Re $[-]$	$1.01^{*}10^{6}$	$0.98^{*}10^{6}$
ω_{red} $[-]$	0.0500	0.0507
α $[^{\circ}]$	8 ± 5.5	8.3 ± 3.5

Table 5.2: *OSU and experimental settings.*

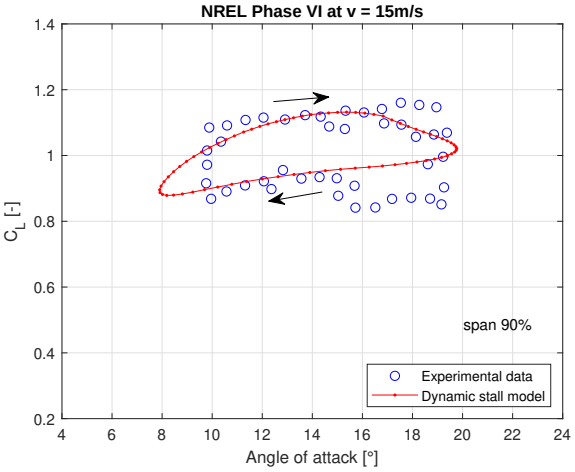

Figure 5.9: *Dynamic stall hysteresis loop.*

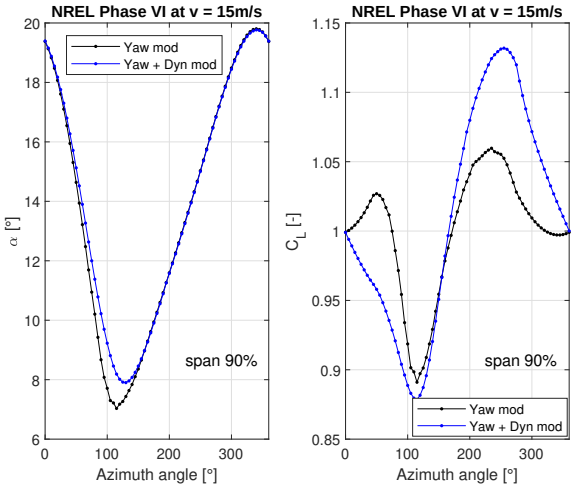

Figure 5.10: *Angle of attack and lift coefficient.*

	OSU testing conditions	Simulation conditions
Re $[-]$	$1.26^{*}10^{6}$	$0.99^{*}10^{6}$
ω_{red} $[-]$	0.0400	0.0424
α $[^{\circ}]$	14 ± 5.5	14.1 ± 5.9

Table 5.3: *OSU and experimental settings.*

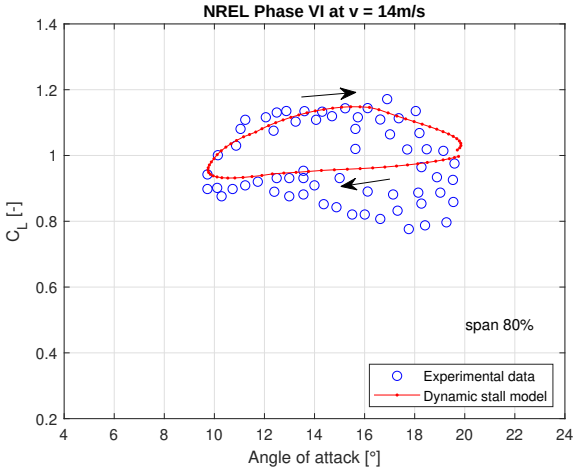

Figure 5.11: *Dynamic stall hysteresis loop.*

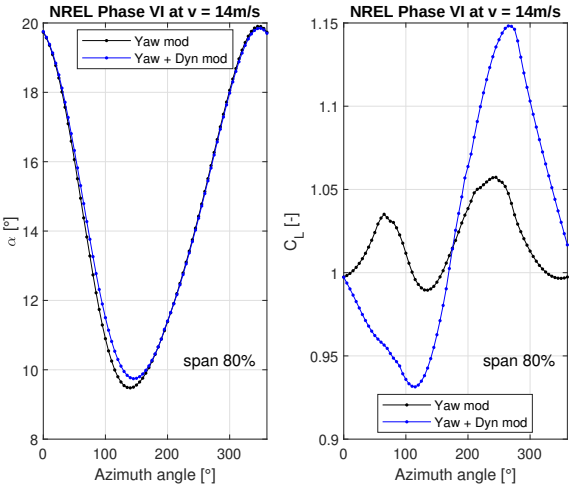

Figure 5.12: *Angle of attack and lift coefficient.*

	OSU testing conditions	Simulation conditions
Re $[-]$	$1.01^{*}10^{6}$	$1.01^{*}10^{6}$
ω_{red} $[-]$	0.0500	0.0507
α $[^{\circ}]$	14 ± 5.5	14.6 ± 5.1

Table 5.4: *OSU and experimental settings.*

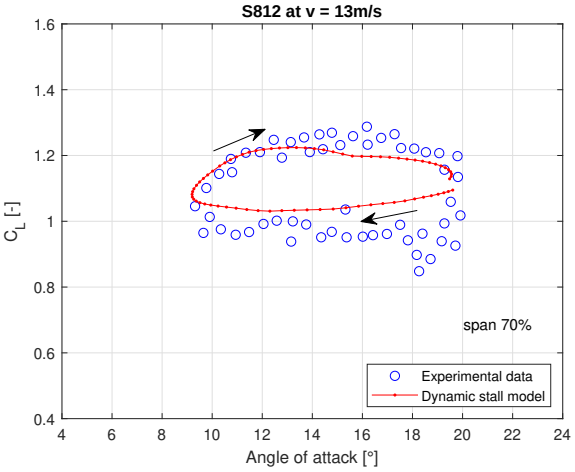

Figure 5.13: *Dynamic stall hysteresis loop.*

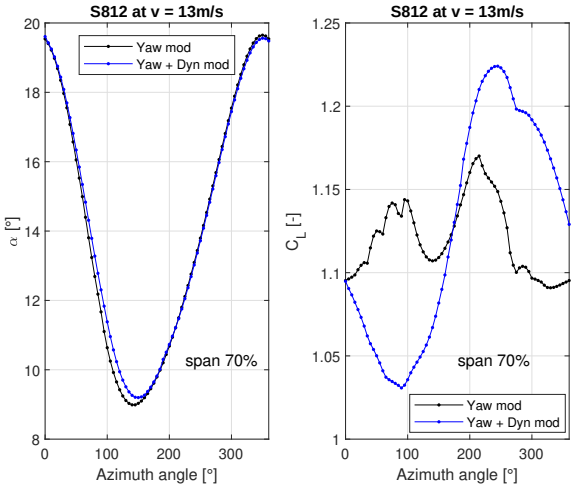

Figure 5.14: *Angle of attack and lift coefficient.*

	OSU testing conditions	Simulation conditions
Re $[-]$	$1.01^{*}10^{6}$	$1.01^{*}10^{6}$
ω_{red} $[-]$	0.0600	0.0606
α $[^{\circ}]$	14 ± 5.5	14.3 ± 5.2

Table 5.5: *OSU and experimental settings.*

As the OSU tested also S812, S813 and S814 airfoils, some simulations have been carried out using these profiles: the same geometrical conditions of chord, radius and twist distributions of NREL Phase VI has been adopted and the S809 airfoil has been replaced with the ones just proposed. The obtained results are represented from Figure 5.13 to Figure 5.20; a good matching between experimental data and calculated lift is achieved by the code, that remarks the ability of Øye's model of well predicting the physical phenomenon.

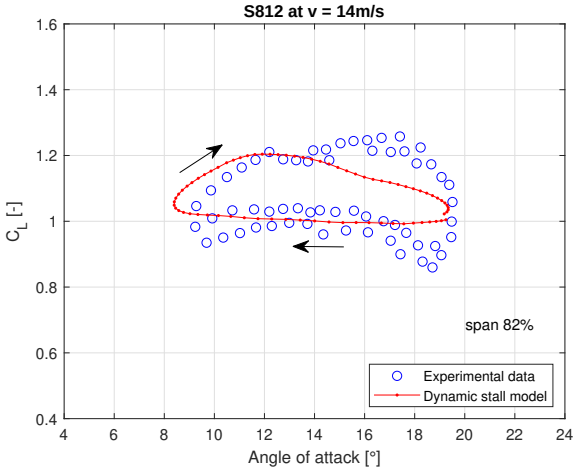

Figure 5.15: *Dynamic stall hysteresis loop.*

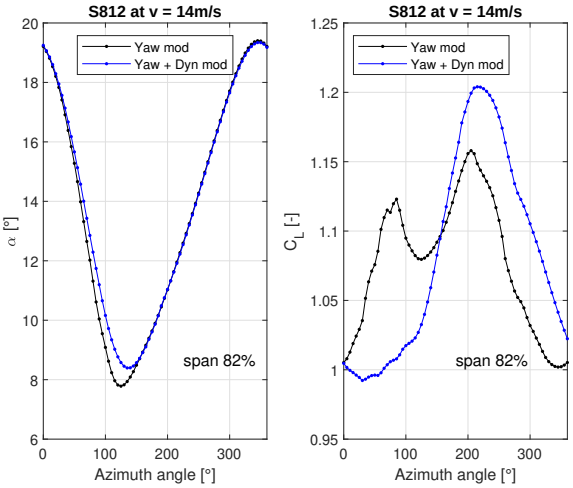

Figure 5.16: *Angle of attack and lift coefficient.*

	OSU testing conditions	Simulation conditions
Re $[-]$	$1.01^{*}10^{6}$	$1.01^{*}10^{6}$
ω_{red} $[-]$	0.0600	0.0606
α $[^{\circ}]$	14 ± 5.5	14.3 ± 5.2

Table 5.6: *OSU and experimental settings.*

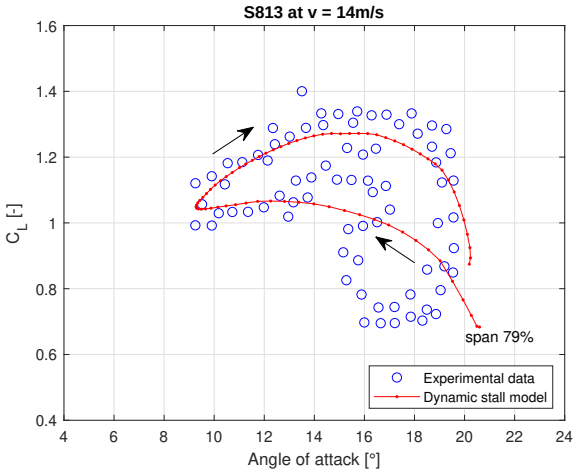

Figure 5.17: *Dynamic stall hysteresis loop.*

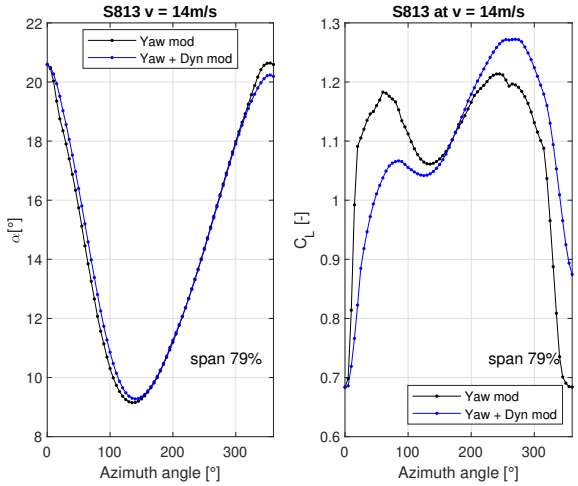

Figure 5.18: *Angle of attack and lift coefficient.*

	OSU testing conditions	Simulation conditions
Re $[-]$	$1.01^{*}10^{6}$	$1.02^{*}10^{6}$
ω_{red} $[-]$	0.0520	0.0516
α $[^{\circ}]$	14 ± 5.5	14.6 ± 5.7

Table 5.7: *OSU and experimental settings.*

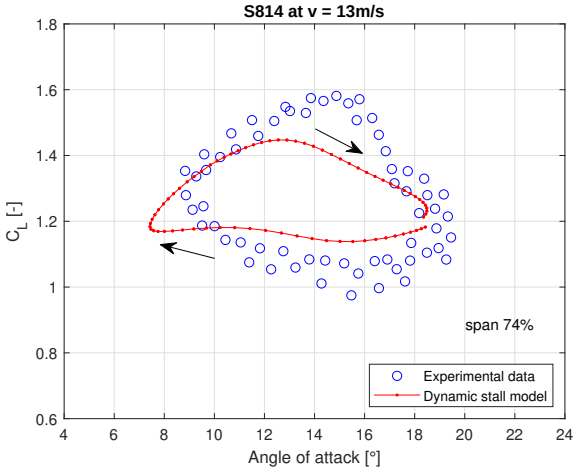

Figure 5.19: *Dynamic stall hysteresis loop.*

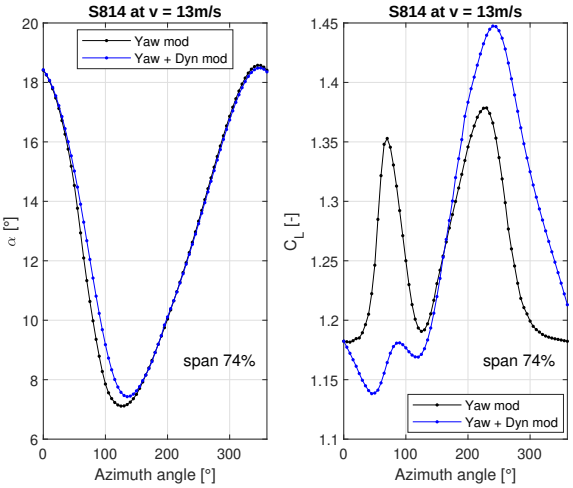

Figure 5.20: *Angle of attack and lift coefficient.*

	OSU testing conditions	Simulation conditions
Re $[-]$	$9.90{*}10^6$	$1.01{*}10^6$
ω_{red} $[-]$	0.0550	0.0564
α $[^\circ]$	14 ± 5.5	13.1 ± 5.5

Table 5.8: *OSU and experimental settings.*

5.2.3 Torque and normal force results

A comparison between the results of Chapter 4 and the present ones with the addition of the dynamic stall model is reported in the following subsection. The same correction for $\theta_{yaw} = 30°$ has been applied to fit the medium values of the experimental data of low speed shaft torque, as mentioned in Chapter 4. Some of the main limits of the yaw models have been discussed in Chapter 4, so a good matching of experimental data in yawed flow is clearly influenced by the accuracy of the selected yaw model. Furthermore, the previous validation of dynamic lift coefficient has just established the robustness and validity of the adopted mathematical model. Therefore, the proposed comparison focuses on the physical effects of the dynamic stall, in particular, on the increased torque value that is expected after the introduction of the dynamic stall. All the proposed models for yawed flow have been tested and coupled with the dynamic stall routine. Results reported in the following subsection refer to the yaw model by Øye, unless otherwise stated.

The differences due to the introduction of dynamic stall model are represented in Figure 5.21 at wind speed $7m/s$: the presence of dynamic stall seems to have a damping effect on the low speed shaft torque, that leads to an underestimation of the maximum torque. Figure 5.22 shows that the dynamic stall does provide similar lift coefficients than the static ones; for example, the hysteresis loop is not so large, as Figure 5.23 represents: an increasing value of torque does not occur, since the stall does not appear at this wind speed.

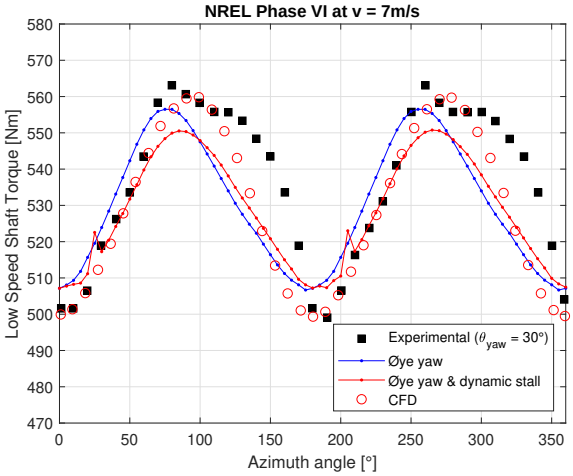

Figure 5.21: *Low speed shaft torque at $7m/s$ with different models activated.*

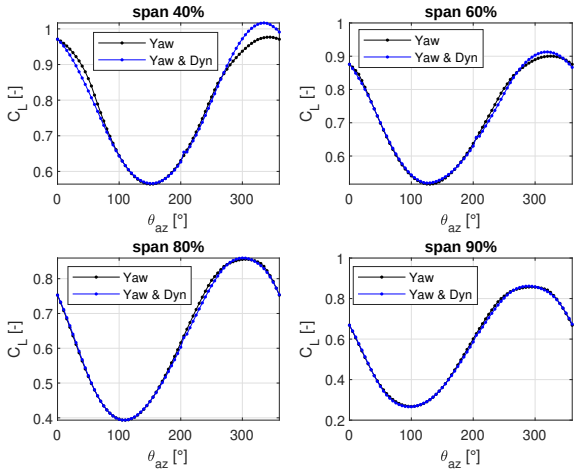

Figure 5.22: *Comparison of lift coefficient with different models activated.*

Figure 5.24 and Figure 5.25 represent the low speed shaft torque and lift coefficients during a complete revolution of the blade at $10m/s$. For medium and high wind speed, the presence of dynamic stall brings to greater value of the torque, as physically expected, and introduces a correct phase shift in the power curve. The dynamic stall model proposed by Øye gives clearly different lift coefficients than the static ones, as depicted in Figure 5.25. Similar considerations can be carried out for results at $15m/s$, whose plots are reported from Figure 5.26 to Figure 5.27. Finally, normal force values are represented from Figure 5.28 to Figure 5.35.

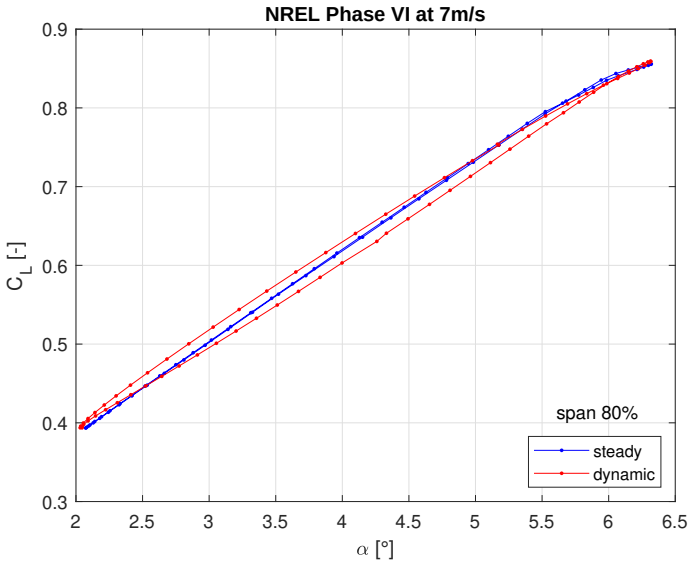

Figure 5.23: *Steady and dynamic lift coefficients.*

Finally, the opportunity to use the dynamic stall model appears only in case of stalled flow, this implies that the routine has to be switched off at low wind speeds.

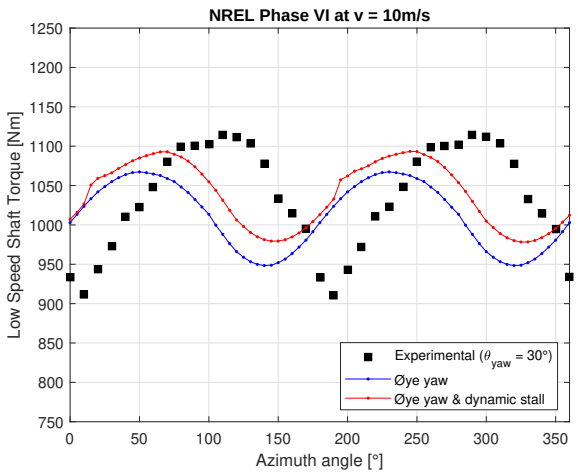

Figure 5.24: *Low speed shaft torque at* $10m/s$ *with different models activated.*

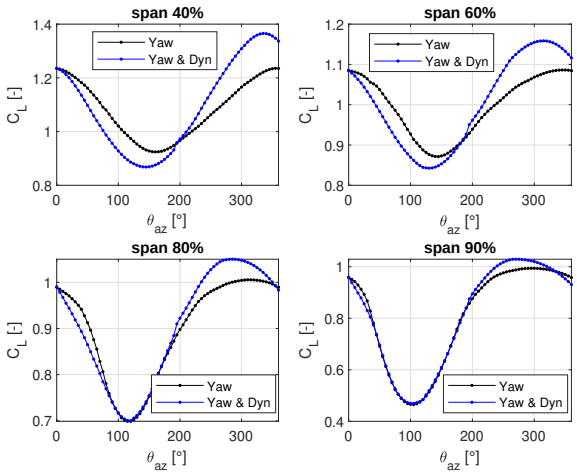

Figure 5.25: *Comparison of lift coefficient with different models activated.*

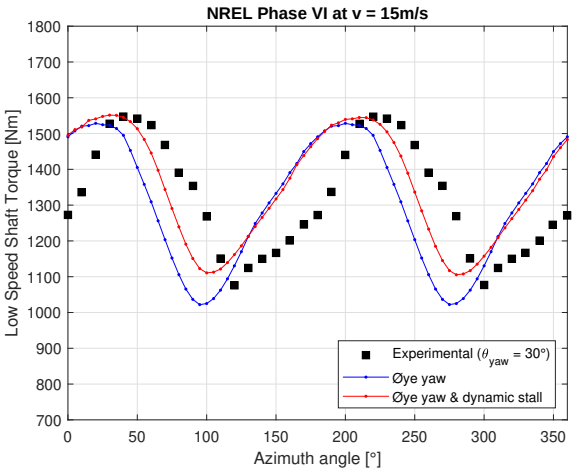

Figure 5.26: *Low speed shaft torque at 15m/s with different models activated.*

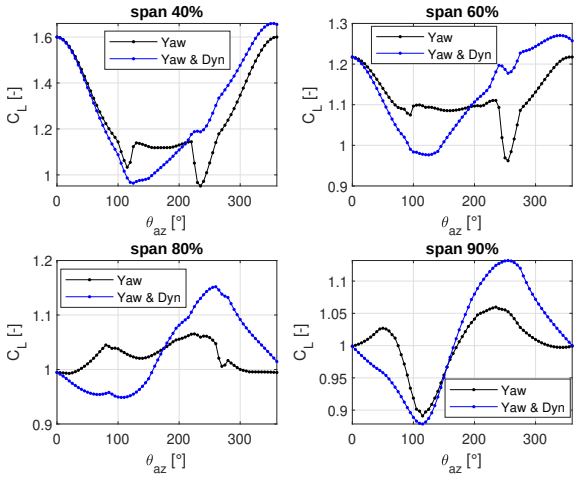

Figure 5.27: *Comparison of lift coefficient with different models activated.*

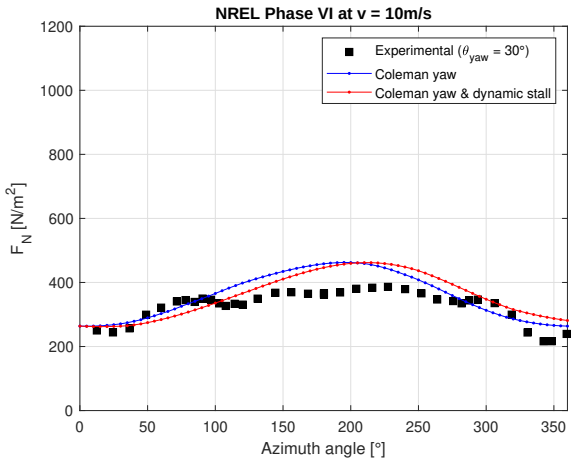

Figure 5.28: *span 47%.*

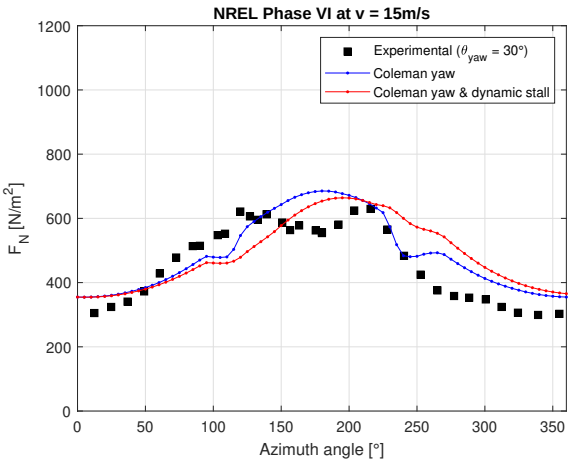

Figure 5.29: *span 47%.*

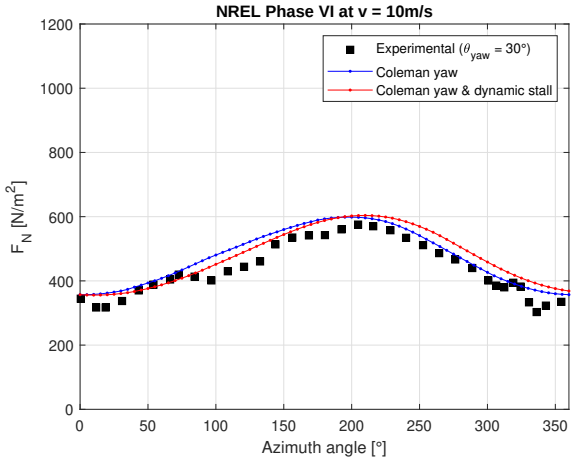

Figure 5.30: *span 63%.*

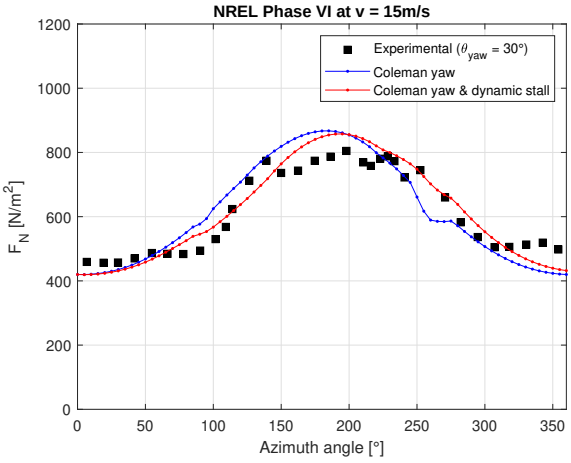

Figure 5.31: *span 63%.*

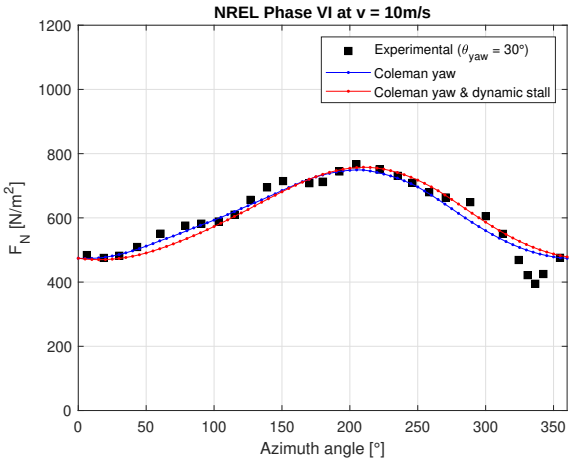

Figure 5.32: *span 80%.*

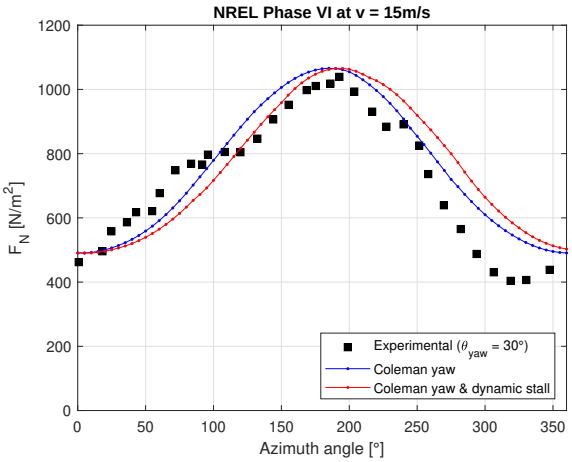

Figure 5.33: *span 80%.*

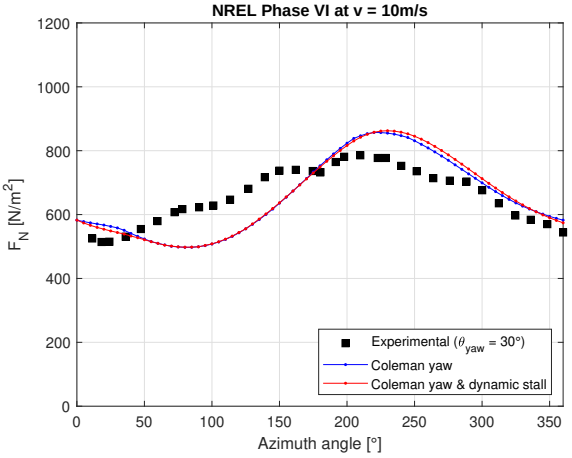

Figure 5.34: *span 95%.*

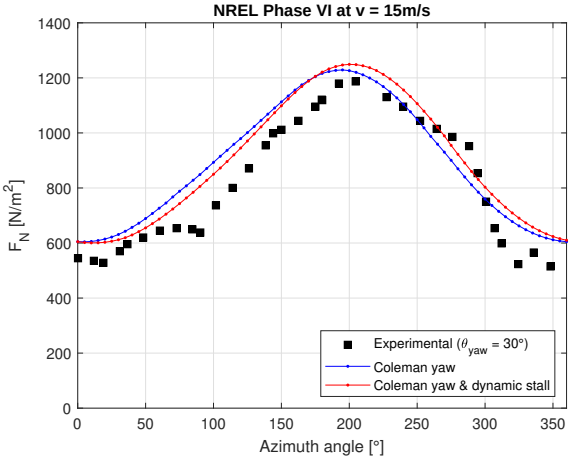

Figure 5.35: *span 95%.*

Conclusions

In the present work improvements and development of a BEM code have been discussed and implemented using MATLAB as development environment: the objectives of a wide database of polar diagrams, a yaw model and a dynamic stall routines have been achieved successfully. The upgrade have endowed the BEM code of a Reynolds interpolation routine, coupled with a large database of polars which provides the correct value of lift and drag coefficients to the blade section, according to its proper Reynolds number. The validation has pointed out an optimum matching between the experimental power curve and the simulation results for AOC 15/50 and NREL Phase VI horizontal axis wind turbines.

Then, the sources of unsteady phenomena have been investigated and a general structure of an unsteady BEM algorithm has been implemented by providing the steady BEM code of yaw and dynamic stall routines. A comparison between the main yaw models has been carried out during the validation. The normal force is well predicted according to most of the yaw models, whereas experimental data on the low speed shaft torque shows some discrepancies in its mean value and for higher wind speeds also in the phase. Furthermore, other differences appear in the amplitude of the oscillating torque curve between each yaw formulation. These discrepancies shows some lacks in the mathematical modelling of the skewed wake geometry, which may be deeper understood using the Computational Fluid Dynamics (CFD).

The last step was the development of the dynamic stall model proposed by Øye. The computated dynamic lift coefficients have been compared to measurements of four oscillating airfoils. The proposed validation has granted successful results, as the calculated hysteresis loops matched the experimental ones. Although dynamic stall involves highly non-linear flow behaviour, the validation has shown the accuracy and robustness of the approach by Øye. The presence of a dynamic stall model in the code has pointed out an increasing trend in power output, especially at high wind speeds.

The forthcoming update to the unsteady BEM code is the development of a dynamic inflow model to account for the time delay before the equilibrium between aerodynamic loads and the wake. Next works may research on advanced simulation techniques, as CFD, to obtain some analytical relationships in order to improve the 1D yaw models currently available. Since the vibrating blades change the relative velocity of the airflow, the code may be coupled with a structural solver to achieve a complete aeroelastic analysis of the wind turbine, which would grant useful results also for stall-induced vibrations, extreme deformations and fatigue assessment.

The importance of low-fidelity calculation tools appears in the early stages of the blade design, as these models allow to obtain accurate global performance results, such as thrust, torque and power, using a low computational cost. For these reasons, benefits of BEM method also appear for structural analysis, preliminary analysis of complex problems (*e.g.* floating wind turbines) and if optimization algorithms are involved in the design process.

Bibliography

[1] A. Dal Monte, S. De Betta, M. Raciti Castelli, E. Benini. Proposal for a coupled aerodynamic–structural wind turbine blade optimization. *Composite Structures, 159, 144–156*, 2017.

[2] https://windeurope.org/wp-content/uploads/files/about-wind/statistics/WindEurope Annual-Statistics-2018.pdf.

[3] M.O.L. Hansen. Aerodynamics of Wind Turbines. *Earthscan*, 2008.

[4] H. Glauert. Airplane propellers. *Aerodynamic theory, In: Durant WF, editor. New York: Dover Pubblications*, 1963.

[5] M.O.L. Hansen, J.N. Sørensen, S. Voutsinas, N. Sørensen, H.Aa. Madsen. State of art in wind turbine aerodynamics and aeroelasticity. *Progress in Aerospace Sciences, 42, 285-330*, 2006.

[6] Jr. Buhl, M.L. A New Empirical Relationship Between Thrust Coefficient and Induction Factors for Turbolent State. *Technical Report NREL/TP-500-36834*, 2005.

[7] http://airfoiltools.com.

[8] S.A. Ning. AirfoilPrep.py Documentation Release 0.1.0. *Technical Report, NREL/TP-5000-58817, 1-15*, 2013.

[9] R. Jacobson, M. Meadors, E. Jacobson, H. Link. Power Performance Test Report for the AOC 15/50 Wind Turbine, Test B. *National Renewable Energy Laboratory, Revision 3*, 2003.

[10] M.M Hand, D.A. Simms, L.J. Fingersh, D.W. Jager, J.R. Cotrell, S. Schreck, S.M. Larwood. Unsteady Aerodynamics Experiment Phase VI: Wind Tunnel Test Configurations and Available Data Campaigns. *NREL National Renewable Energy Laboratory*, 2001.

[11] L. Menegozzo, A. Dal Monte, E. Benini, A. Benato. Small wind turbines: A numerical study for aerodynamic performance assessment under gust conditions. *Renewable Energy, 121, 123-132*, 2018.

[12] H. Glauert. A General Theory for the Autogiro. *ARC R M, 786*, 1926.

[13] D. Micallef, T. Sant. A Review of Wind Turbine Yaw Aerodynamics. *Wind Turbine - Design, Control and Applications, Chapter 2, 27-53*, 2016.

[14] F. Blondel, G. Ferrer, M. Cathelain, D. Teixeira. Improving a BEM Yaw Model Based on NewMexico Experimental Data and Vortex/CFD Simulations. *IFP Energies Nouvelles, 23ème Congrès Français de Mécanique*, 2017.

[15] X. Chen, S. Kang. Numerical Simulation of the Unsteady Aerodynamic of Wind Turbine under Yaw Condition. *Advanced Materials Research, Vols. 1070-1072, 1883-1887*, 2015.

[16] T. Sant, G. van Kuik, G. van Bussel. Estimating the Unsteady Angle of Attack from Blade Pressure Measurements in the NREL Phase VI Rotor in Yaw using a Free-Wake Vortex Model. *American Institute of Aeronautics and Astronautics, 44, 393*, 2006.

[17] K. Ryu, Y. Seo, W. Lee. Prediction of Aerodynamic Loads for NREL Phase VI Wind Turbine Blade in Yawed Condition. *International Journal of Aeronautical and Space Sciences, 17(2), 157-166*, 2016.

[18] J. Chen, X. Shen, X. Zhu, Z. Du. Influence of wake asymmetry on wind turbine blade aerodynamic and aeroelastic performance in shear/yawed wind. *Journal of Renewable and Sustainable Energy, 10*, 2018.

[19] M.H. Hansen, M. Gaunaa, H.A. Madsen. A Beddoes-Leishman type dynamic stall model in state-space and indicial formulations. *Risø National Laboratory, Roskilde, Denmark*, 2004.

[20] Ohio R. Reuss Ramsay, M.J. Hoffmann, G.M. Gregorek, The Ohio State University Columbus. Effects of Grit Roughness and Pitch Oscillations on the S809 Airfoil. *Airfoil Performance Report, Revised(12/99), NREL/TP-442-7817*, 1995.

[21] Ohio R. Reuss Ramsay, M.J. Hoffmann, G.M. Gregorek, The Ohio State University Columbus. Effects of Grit Roughness and Pitch Oscillations on the S809 Airfoil. *Airfoil Performance Report, Revised(12/99), NREL/SR-440-8167*, 1998.

[22] Ohio R. Reuss Ramsay, M.J. Hoffmann, G.M. Gregorek, The Ohio State University Columbus. Effects of Grit Roughness and Pitch Oscillations on the S809 Airfoil. *Airfoil Performance Report, Revised(12/99), NREL/TP-442-8168*, 1996.

[23] Ohio R. Reuss Ramsay, M.J. Hoffmann, G.M. Gregorek, The Ohio State University Columbus. Effects of Grit Roughness and Pitch Oscillations on the S809 Airfoil. *Airfoil Performance Report, Revised(12/99), NREL/TP-442-8161*, 1996.

[24] M.A. Khan. Dynamic Stall Modeling for Wind Turbines. *Master Degree of Science at the Delft University of Technology*, 2018.

[25] R. Pereira, G. Schepers, M.D. Pavel. Validation of the Beddoes-Leishman dynamic stall model for horizontal axis wind turbines using MEXICO data. *Wind Energy, 16(2)*, 2013.